Received: Added at production | Revised: Added at production | Accepted: Added at production

DOI: xxx/xxxx

RESEARCH ARTICLE

A computationally tractable framework for nonlinear dynamic multiscale modeling of membrane fabric

Philip Avery[1] | Daniel Z. Huang[3] | Wanli He[2] | Johanna Ehlers[2] | Armen Derkevorkian[4] | Charbel Farhat[1,2,3]

[1]Department of Aeronautics and Astronautics, Stanford University, Stanford, CA 94305, USA
[2]Department of Mechanical Engineering, Stanford University, Stanford, CA 94305, USA
[3]Institute for Computational and Mathematical Engineering, Stanford University, Stanford, CA 94305, USA
[4]Jet Propulsion Laboratory, California Institute of Technology, Pasadena, CA 91109, USA

Summary

A general-purpose computational homogenization framework is proposed for the nonlinear dynamic analysis of membranes exhibiting complex microscale and/or mesoscale heterogeneity characterized by in-plane periodicity that cannot be effectively treated by a conventional method, such as woven fabrics. The proposed framework is a generalization of the "Finite Element squared" (or FE^2) method in which a localized portion of the periodic subscale structure – typically referred to as a Representative Volume Element (RVE) – is modeled using finite elements. The numerical solution of displacement-driven problems using this model furnishes a mapping between the deformation gradient and the first Piola-Kirchhoff stress tensor. This unconventional material model can be readily applied in the context of membranes by using a variant of the approach proposed by Klinkel and Govindjee [1] for using conventional, finite strain, three-dimensional material models in beam and shell elements. The approach involves the numerical enforcement of the plane stress constraint, which is typically performed on out-of-plane components of the second Piola-Kirchhoff stress tensor ($\boldsymbol{S}$). Observing the principal of frame invariance, the RVE solution is reinterpreted as a mapping between the right stretch tensor and the symmetric Biot stress tensor conjugate pair. This facilitates the development of a drop-in replacement for any conventional finite strain plane stress material model formulated in terms of the in-plane components of the Green-Lagrange strain tensor and $\boldsymbol{S}$. Finally, computational tractability is achieved by introducing a regression-based surrogate model to avoid further solution of the RVE model when data sufficient to fit a model capable of delivering adequate approximations is available. For this purpose, a physics-inspired training regimen involving the utilization of our generalized FE^2 method to simulate a variety of numerical experiments – including but not limited to uniaxial, biaxial and shear straining of a material coupon – is proposed as a practical method for data collection. The proposed framework is demonstrated for a Mars landing application involving the supersonic inflation of an atmospheric aerodynamic decelerator system that includes a parachute canopy made of a woven fabric. Several alternative surrogate models are evaluated including a neural network.

KEYWORDS:
FE, regression, multiscale, woven fabrics, neural network

1 | INTRODUCTION

Nonlinear multiscale problems – defined here as those nonlinear problems that exhibit vastly different scale features that are significant to the macroscopic behavior – are ubiquitous in science and engineering. They arise, for example, in the modeling of woven fabrics (see Figure 1) used in body armor and inflatable structures such as vehicle air bags, parachutes and other atmospheric decelerators. Numerical methods that attempt to resolve all relevant scales can lead to massive discretized problems. However, recent developments using a variety of alternative surrogate modeling techniques – including nonlinear model order reduction[2,3], kriging[4], and neural networks[5,6] – to accelerate the solution of one or more scales within the context of a computational homogenization framework present a coherent methodology by which a computationally tractable approximation can be attained without resorting to ad-hoc approximations. Notably, thin shell and membrane discretizations have not been considered in this context prior to this work although several frameworks for multiscale modeling of shells without emphasis on computational efficiency have been proposed[7,8,9]. In particular we will address the case of a *hybrid* discretization in which plane stress membrane elements are employed for the sake of convenience and numerical efficiency at the macroscopic scale, while three-dimensional solid elements are preferred for the sake of generality and in order to most precisely represent geometric features and deformation modes at the mesoscopic and/or microscopic scales.

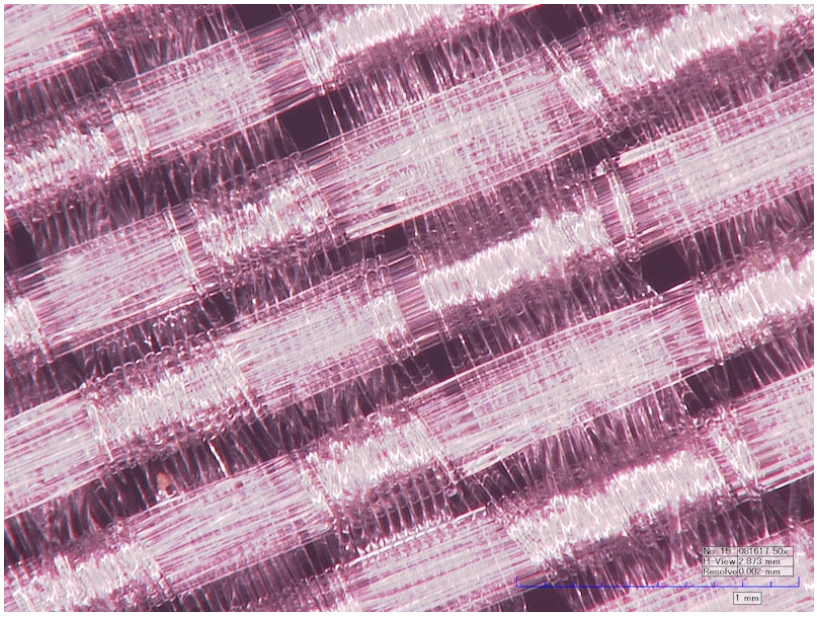

FIGURE 1 Optical microscope imaging of parachute membrane fabric yarns under tensile loading.

We choose to build our framework on a macro-micro concept that generalizes to n-levels, although without loss of generality we present only the two-level case here anticipating that this case can be sufficient for many problems of interest. The framework allows for the treatment of unilateral contact constraints at both macroscale and microscale. We propose using a microscale model discretized with solid elements to allow accurate representation of microscopic geometric features such as yarns and voids. However, the proposed framework readily generalizes to alternative microscale discretizations such as shell elements. For the case of a macroscale model that is also discretized with solid elements, well-established localization/homogenization scale bridging strategies have been developed[10] and typically provide a mapping between the *three-dimensional* deformation gradient ($\boldsymbol{F}$) and first Piola-Kirchhoff stress ($\boldsymbol{P}$) tensors from which a constitutive relation is inferred. However, when the macroscale model is discretized with membrane elements and the microscale is discretized with solid elements then coupling between the two scales requires careful attention. The proposed treatment has two novel components.

- First, we observe that due to the principal of material frame invariance the conventional three-dimensional $\boldsymbol{F}$–$\boldsymbol{P}$ scale bridging approach can be reformulated using the polar decomposition of the deformation gradient to furnish a mapping

between the right stretch tensor and its conjugate, the symmetric Biot stress tensor. Using this reformulation combined with some straightforward transformations, we will show that an unconventional FE^2 material model can *conveniently* be used as a drop-in replacement for any conventional three-dimensional material model formulated as a mapping between the commonly used Green-Lagrange strain ($\boldsymbol{E}$) and its conjugate, the second Piola-Kirchhoff stress tensor ($\boldsymbol{S}$). The relevance of this development to the issue of multiscale membrane-solid coupling will be addressed in what follows.

- Material models used in membrane elements are typically of the plane stress variety. In some cases, a plane stress variant of a three-dimensional material model can be derived for which the plane stress condition is enforced analytically. When an analytical solution is not available, numerical enforcement of the plane stress condition is commonly used, for example in the case of J2 elastoplasticity [11]. This involves solving numerically – with a root-finding method such as Newton's method or the bisection method – a nonlinear equation to enforce the plane stress condition. Klinkel and Govindjee have shown [1] how numerical enforcement of the plane stress condition can be used to construct an interface that in principle enables any three-dimensional material model to be "converted" into a plane stress variant which can then be used in a shell or beam element. However, the plane stress condition is typically expressed by constraints on the out-of-plane components of the *second Piola-Kirchhoff* stress tensor, so the method of Klinkel and Govindjee is presented by the authors in the most convenient way using the $\boldsymbol{E}$–$\boldsymbol{S}$ conjugate pair. We simply observe that the method of Klinkel and Govindjee can be trivially adapted to membranes and furthermore can be conveniently used with any material model of the form $\boldsymbol{S} = \hat{\boldsymbol{S}}(\boldsymbol{E})$ including, but not limited to, constitutive relations inferred from a FE^2 computational homogenization formulated using the polar decomposition as described previously.

Motivated by the fact that the proposed plane stress constitutive law is essentially a mapping is between two pairs of 3-dimensional vectors, we consider a lightweight alternative in which a regression based-model is used as a surrogate for constitutive function evaluations that would otherwise require solution of a finite-element model of the microscale RVE. Three alternative surrogates each capable of achieving computational tractability are presented and evaluated: (1) the classical linear elastic model fitted to data using linear regression, (2) a quadratic model fitted to data using linear regression, and (3) an artificial neural network model fitted to data using the PyTorch library. In each case the data used to train and test the model is obtained by exercising the proposed high-fidelity multiscale membrane model on a series of numerical experiments intended to mimic the familiar physical experimental-based methodology typically used in the development of conventional material models.

The remainder of this paper is organized as follows. Section 2 provides an overview of the proposed two-level multiscale framework with a locally attached microscale, focusing on the context of large-deformation structural mechanics with macroscopic discretization using membrane elements, microscale discretization using 3D solid elements, bridging between the scales, and the solution of the discrete coupled multiscale problem including treatment of contact at both scales. In Section 3, three regression-based surrogate microscale models and their training methodologies are presented and compared. A numerical example is provided in Section 4 to evaluate the proposed framework, involving a realistic simulation of the deployment of a Disk-Gap-Band (DGB) parachute in the Martian atmosphere. Finally, we offer conclusions in Section 5.

2 | LOCALLY ATTACHED MICROSTRUCTURE MULTISCALE FORMULATION FOR MEMBRANES

In this section, a multiscale continuum mechanics formulation suitable for membranes based on the concept of a locally attached microstructure is presented. As formulated, the stress-strain relationship for a heterogeneous membrane is not defined by a conventional plane stress constitutive law but rather by (a) the solution at each material point of one or more boundary value problems governing its microstructure, and (b) the numerical enforcement of the plane stress condition. Although the concept generalizes naturally to three or more scales, for simplicity it is applied here to address problems that exhibit precisely two separate scales. Specifically, the stress-strain relationship at the coarse scale is defined by the solution of the boundary value problems at the fine scale, an appropriate scale transition method, and a constraint on the out-of-plane components of the homogenized stress tensor. At the finest scale, where all heterogeneities can be adequately resolved and described by an available constitutive theory, it is defined by an analytical constitutive law. All considered length scales are assumed to be much larger than the molecular dimension so that the continuum assumption holds. Furthermore, scale separation is assumed to loosely couple the various scales through localization from coarse to fine scales and homogenization from fine to coarse scales. For further details, the reader is referred to [12,10,13,14] for the concept of a locally attached microstructure. The approach adopted here

can be interpreted as a kind of generalization and/or application to the case of membranes of the localization/homogenization scale bridging strategy presented in [10].

2.1 | Preliminaries

Consider a domain $\mathscr{B}_0 \subset \mathbb{R}^3$ that defines a highly heterogeneous membrane structure of interest. Assume that its boundary $\partial\mathscr{B}_0$ is subject to prescribed displacements on $\partial\mathscr{B}_0^{\boldsymbol{u}} \subset \partial\mathscr{B}_0$, and tractions on $\partial\mathscr{B}_0 \setminus \partial\mathscr{B}_0^{\boldsymbol{u}}$. Let $\boldsymbol{\varphi}_0^t : \mathscr{B}_0 \to \mathscr{B}_0^t$ denote the nonlinear transformation that maps a point in the reference configuration, $\boldsymbol{X}_0 \in \mathscr{B}_0$, at time t to a counterpart in the current configuration, $\boldsymbol{x}_0(\boldsymbol{X}_0; t) = \boldsymbol{\varphi}_0^t(\boldsymbol{X}_0) \in \mathscr{B}_0^t$. The current configuration of the membrane $\mathscr{B}_0^t$ is assumed to be defined as

$$\mathscr{B}_0^t = \{\boldsymbol{x}_0 \in \mathbb{R}^3 \mid \boldsymbol{x}_0 = \boldsymbol{\phi}\left(\xi^{(1)}, \xi^{(2)}\right) + \xi^{(3)}\boldsymbol{n}_0\}$$

where the map $\boldsymbol{\phi} : \mathscr{A}_0 \to \mathbb{R}^3$ defines the current position of the mid-surface of the membrane, $(\xi^{(1)}, \xi^{(2)}) \in \mathscr{A}_0 \subset \mathbb{R}^2$ are coordinates parameterizing the mid-surface, $\boldsymbol{n}_0 \in \mathbb{R}^3$ is the unit normal to the mid-surface in the current configuration, $\xi^{(3)} \in \left[-h/2, h/2\right]$ is a coordinate parameterizing the direction normal to the surface, and h is the upper bound of the membrane thickness. Similarly, the reference configuration of the membrane $\mathscr{B}_0$ is defined as

$$\mathscr{B}_0 = \{\boldsymbol{X}_0 \in \mathbb{R}^3 \mid \boldsymbol{X}_0 = \boldsymbol{\Phi}\left(\xi^{(1)}, \xi^{(2)}\right) + \xi^{(3)}\boldsymbol{N}_0\}$$

where the the map $\boldsymbol{\Phi} : \mathscr{A}_0 \to \mathbb{R}^3$ defines the reference position of the mid-surface of the membrane, and $\boldsymbol{N}_0 \in \mathbb{R}^3$ is the unit normal to the mid-surface in the reference configuration. The deformation of this domain is governed by a reduction of the finite deformation continuum equations to the mid-surface with a plane stress but otherwise unknown constitutive law due to the assumed highly heterogeneous fine scale structure. For this reason, generalizing the work described in [12,10,13,14], the deformation problem is solved here by locally attaching an appropriately defined microstructure to each mid-surface point, computing the stress-strain relationship at each such point through the solution of a microstructure boundary value problem, bridging the scales via a localization and homogenization strategy, and numerically enforcing the plane stress constraint on the resulting homogenized stress tensor. An appropriately defined microstructure in this context is one that represents only a minuscule "Representative Surface Element" (RSE) of the membrane within which the entire thickness of the membrane is represented in its entirety. Hence, the range of the in-plane coordinates $\xi^{(1)}, \xi^{(2)}$ in the microscale domain should be much smaller than in the macroscale domain, while the ranges of the normal coordinate $\xi^{(3)}$ should be identical in both domains. The separation of scales and assumed periodicity in only two of the three spatial dimensions is a notable characteristic of the problem of interest and its proposed treatment that distinguishes it from the ubiquitous alternative multiscale treatments devised for fully three-dimensional scale bridging.

Here and throughout the remainder of this paper, the subscripts 0 and 1 denote quantities associated with the coarse (0-th) and fine (1-st) scales, respectively. For simplicity, a k-th scale is also referred to as scale k or level k, interchangeably. The deformation at both scales is governed by the finite deformation continuum equations, with the stress-strain relationship defined by the solution of a constrained boundary value problem formulated at a finer scale for level $k = 0$, or an assumed constitutive law at the fine scale designated by level $k = 1$. Let $\boldsymbol{\varphi}_1 : \mathscr{B}_1 \to \mathscr{B}_1'$ denote the nonlinear transformation that maps a point in the fine scale reference configuration, $\boldsymbol{X}_1 \in \mathscr{B}_1$, to a counterpart in the fine scale current configuration, $\boldsymbol{x}_1(\boldsymbol{X}_1) = \boldsymbol{\varphi}_1(\boldsymbol{X}_1) \in \mathscr{B}_1'$. As in the formulation of the macroscale problem, we define $\partial\mathscr{B}_1$ as the boundary of $\mathscr{B}_1$ and $\partial\mathscr{B}_1^{\boldsymbol{u}}$ as its part where a displacement is prescribed.

The boundary conditions at scale 0 are defined by the physical problem of interest, while those at scale 1 depend on the deformations at the coarse scale. The constitutive law at the fine scale is chosen based on the expected response of this scale, while at the coarse scale there is no preassigned constitutive law but rather a dependence on the microstructure response to evaluate the constitutive function. Arbitrarily complex fine scale constitutive relationships involving nonlinearities and path-dependency are allowed and described here by

$$\boldsymbol{S}_1 = \hat{\boldsymbol{S}}_1\left(\boldsymbol{E}_1, \boldsymbol{\Xi}_1\right)$$

where $\boldsymbol{S}_1$, $\boldsymbol{E}_1$ and $\boldsymbol{\Xi}_1$ denote the microscale second Piola-Kirchhoff stress tensor, Green-Lagrange strain tensor and history variables, respectively, and $\hat{\boldsymbol{S}}_1$ is the microscale constitutive function. At the coarse scale we wish to devise a multiscale, plane stress constitutive function of the form

$$\boldsymbol{S}_0^m = \hat{\boldsymbol{S}}_0^m\left(\boldsymbol{E}_0^m, \boldsymbol{\Xi}_0\right) \tag{1}$$

where $\boldsymbol{S}_0$, $\boldsymbol{E}_0$ and $\boldsymbol{\Xi}_0$ denote the macroscale second Piola-Kirchhoff stress tensor, Green-Lagrange strain tensor and history variables, respectively. The subscript m applied to a *tensor* quantity (for example $\boldsymbol{S}_0^m$ and $\boldsymbol{E}_0^m$) denotes a restriction of the tensor

to its in-plane membrane components. For example, the membrane part of $\boldsymbol{S}_0$ is given by

$$\boldsymbol{S}_0^m = \begin{bmatrix} S_0^{(11)} & S_0^{(12)} \\ S_0^{(21)} & S_0^{(22)} \end{bmatrix}$$

The superscript m applied to a *constitutive function* (for example $\hat{\boldsymbol{S}}_0^m$) indicates that the function is a particular plane stress type of constitutive relation that evaluates the in-plane membrane components of a stress tensor while constraining the out-of-plane components to be zero. A general numerical procedure used to construct this function will be defined subsequently.

2.2 | Scale bridging

Following the work presented in [10], the boundary conditions on $\mathscr{B}_1$ are defined so that the pointwise deformation gradient tensor at level 0, $\boldsymbol{F}_0$, is equal to the volumetric average of the deformation gradient tensor at level 1

$$\boldsymbol{F}_0 = \frac{1}{|\mathscr{B}_1|} \int_{\mathscr{B}_1} \boldsymbol{F}_1 \, dV$$

This *localization* transmission condition can be conveniently enforced by prescribing a boundary deformation of the form

$$\boldsymbol{x}_1\big|_{\partial\mathscr{B}_1^{\boldsymbol{u}}} = \boldsymbol{X}_1\big|_{\partial\mathscr{B}_1^{\boldsymbol{u}}} \boldsymbol{F}_0 + \boldsymbol{w}_1 \tag{2}$$

subject to some conditions (see [2]), where $\boldsymbol{w}_1$ represents the non-uniform part of the boundary deformation. Without loss of generality, in this work we assume uniform essential boundary conditions defined by the condition $\boldsymbol{w}_1 = 0$.

The pointwise first Piola-Kirchhoff stress tensor at level 0 is defined as the volumetric average of the stress tensor at level 1

$$\boldsymbol{P}_0 = \frac{1}{|\mathscr{B}_1|} \int_{\mathscr{B}_1} \boldsymbol{P}_1 \, dV \tag{3}$$

This *homogenization* transmission condition can be conveniently determined from quantities defined solely on $\partial\mathscr{B}_1^{\boldsymbol{u}}$ by applying a Gauss-type identity to (3)

$$\boldsymbol{P}_0 = \frac{1}{|\mathscr{B}_1|} \int_{\partial\mathscr{B}_1^{\boldsymbol{u}}} \boldsymbol{P}_1 \boldsymbol{N}_1 \otimes \boldsymbol{X}_1 \, dA \tag{4a}$$

$$= \frac{1}{|\mathscr{B}_1|} \boldsymbol{X}_1^T\big|_{\partial\mathscr{B}_1^{\boldsymbol{u}}} \boldsymbol{f}_1\big|_{\partial\mathscr{B}_1^{\boldsymbol{u}}} \tag{4b}$$

where $\boldsymbol{f}_1\big|_{\partial\mathscr{B}_1^{\boldsymbol{u}}}$ is the vector of so-called *reaction forces* associated with the prescribed deformations (2) and the superscript $\boldsymbol{T}$ designates the transpose operation.

In this context, the microscale volume measure $|\mathscr{B}_1|$ should be interpreted as the entire volume of a bounding box enclosing the microscale volume (see Figure 2) including both regions of solid material and voids. The height of the bounding box $h + \varepsilon$ should be slightly larger than the minimum enclosing dimension h in the $\xi^{(3)}$ direction (i.e. $\varepsilon > 0$) so that the microscale volume $\mathscr{B}_1$ does not intersect with the box's upper and lower faces. The magnitude of ε is otherwise arbitrary as the dependence of the homogenized stress tensor on this parameter will be subsequently canceled when evaluating the membrane stress resultant. Note that the boundary $\partial\mathscr{B}_1^{\boldsymbol{u}}$ used to define the transmission conditions are entirely contained within the four side faces of the bounding box, i.e. the faces whose normals coincide with the $\xi^{(1)}$ and $\xi^{(2)}$ axes.

Equations (2) and (4) constitute a relation of the form

$$\boldsymbol{P}_0 = \hat{\boldsymbol{P}}_0 \left(\boldsymbol{F}_0, \boldsymbol{\Xi}_0 \right) \tag{5}$$

which is evaluated in three steps:

1. First, the microscale problem with prescribed boundary values given by (2) is solved.
2. Next, the solution of the microscale problem is postprocessed to obtain the reaction forces. This can be done either by a boundary integral as shown in (4a), or alternatively by a volume integral over the region of the domain adjacent to the boundary [15].
3. Finally, the reaction forces are combined and scaled according to (4b) to produce the homogenized first Piola-Kirchhoff stress tensor $\boldsymbol{P}_0$.

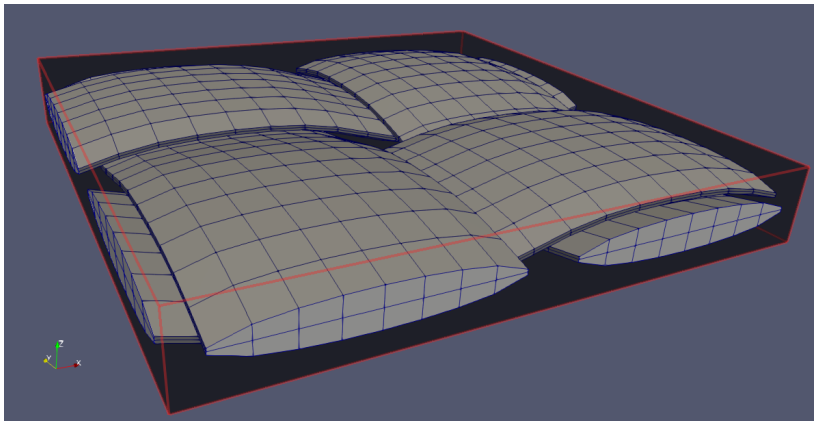

FIGURE 2 Representative Surface Element of the membrane within which the entire thickness of the membrane is represented in its entirety.

Unfortunately, (5) is not directly compatible with the stated application of interest, namely a *plane stress* relation of the form (1) expressed in terms of the in-plane components of the Green-Lagrange strain and second Piola-Kirchhoff stress tensors. To formally adapt the homogenization methodology to this setting, we first assume without loss of generality that relation (5) satisfies the principal of material frame invariance which can be stated as follows [16]

$$\hat{\boldsymbol{P}}_0\left(\boldsymbol{Q}\boldsymbol{F}_0\right) = \boldsymbol{Q}\hat{\boldsymbol{P}}_0\left(\boldsymbol{F}_0\right) \quad \forall\, \boldsymbol{Q} \in SO(3) \tag{6}$$

where $SO(3)$ is the group of special orthogonal transformations defined as

$$SO(3) = \{\boldsymbol{Q} \in \mathbb{R}^3 \,:\, \boldsymbol{Q}^T\boldsymbol{Q} = \boldsymbol{Q}\boldsymbol{Q}^T = \boldsymbol{I},\ \det(\boldsymbol{Q}) = 1\}$$

and $\mathbf{I}$ is the identity matrix. Regarding the assumption of material frame indifference, under some conditions it can be shown that (5) is objective [17] and hence (6) holds. For cases in which (6) does not hold, the proposed alternative formulation which follows can be interpreted as imposing or restoring material frame invariance which is generally considered to be appropriate for constitutive relations in solid mechanics.

Introducing the polar decomposition of the deformation gradient

$$\boldsymbol{F}_0 = \boldsymbol{R}_0\boldsymbol{U}_0$$

where $\boldsymbol{R}_0 \in SO(3)$ is the rotation tensor and $\boldsymbol{U}_0 \in \mathbb{R}^{3\times3}$ is the right stretch tensor which is positive definite and symmetric, and the unsymmetric Biot stress tensor defined as

$$\boldsymbol{B}_0 = \boldsymbol{R}_0^T\boldsymbol{P}_0,$$

it follows from (6) taking $\boldsymbol{Q} = \boldsymbol{R}_0^T$ that the homogenized constitutive law (5) can equivalently be stated as a relation between the right stretch tensor and the unsymmetric Biot stress using the same functional form, i.e.

$$\boldsymbol{B}_0 = \hat{\boldsymbol{P}}_0\left(\boldsymbol{U}_0, \boldsymbol{\Xi}_0\right). \tag{7}$$

This can be interpreted simply as a variant of the standard transmission conditions (2, 4) in which the right stretch tensor is used instead of the deformation gradient to compute the microscale prescribed boundary deformations, and the homogenized stress tensor obtained by evaluating the constitutive function $\hat{\boldsymbol{P}}_0$ is identified as the Biot measure rather than the first Piola-Kirchhoff. Specifically,

$$\boldsymbol{x}_1\big|_{\partial\mathscr{B}_1^{\boldsymbol{u}}} = \boldsymbol{X}_1\big|_{\partial\mathscr{B}_1^{\boldsymbol{u}}}\boldsymbol{U}_0 \tag{8a}$$

$$\boldsymbol{B}_0 = \frac{1}{|\mathscr{B}_1|}\,\boldsymbol{X}_1^T\Big|_{\partial\mathscr{B}_1^{\boldsymbol{u}}}\,\boldsymbol{f}_1\big|_{\partial\mathscr{B}_1^{\boldsymbol{u}}}. \tag{8b}$$

A more convenient relation between the Green-Lagrange strain and the first Piola-Kirchhoff stress tensor can be obtained from (7) by utilizing well-known transformations [18]:

- First, the right stretch tensor can be obtained from the Green-Lagrange strain using

$$\boldsymbol{U}_0 = (\mathbf{C}_0)^{\frac{1}{2}} = \sum_{i=1}^{i=3} \lambda_i N_i \otimes N_i \tag{9}$$

where $\mathbf{C}_0 = 2\boldsymbol{E}_0 + \mathbf{I}$ is the right Cauchy-Green deformation tensor, and λ_i^2 and N_i are the eigenvalues and eigenvectors, respectively, of $\mathbf{C}_0$.

- Second, the second Piola-Kirchhoff stress can be obtained from the Biot stress using

$$0.5\left(\boldsymbol{S}_0\boldsymbol{U}_0 + \boldsymbol{U}_0\boldsymbol{S}_0\right) = \boldsymbol{T}_0 \tag{10}$$

where $\boldsymbol{T}_0$ is the symmetric part of the Biot stress tensor $\boldsymbol{T}_0 = 0.5\left(\boldsymbol{B}_0 + \boldsymbol{B}_0^T\right)$. Note that (10) has the form of the Lyapunov equation whose solution is given by a linear system of equations, namely

$$\text{vec}\left(\boldsymbol{S}_0\right) = \left[\mathbf{I} \otimes \boldsymbol{U}_0 + \boldsymbol{U}_0^T \otimes \boldsymbol{I}\right]^{-1} \text{vec}\left(2\boldsymbol{T}_0\right) \tag{11}$$

where $\otimes$ denotes the Kronecker product, and $\text{vec}\,(\cdot)$ denotes vectorization. For example, vectorization of $\boldsymbol{S}_0$ is given by

$$\text{vec}\left(\boldsymbol{S}_0\right) = \left[S_0^{(11)}\ S_0^{(21)}\ S_0^{(31)}\ S_0^{(12)}\ S_0^{(22)}\ S_0^{(32)}\ S_0^{(13)}\ S_0^{(23)}\ S_0^{(33)}\right]^T.$$

The dimension of Eq. (11) can be reduced further to six due to symmetry.

Substituting (9) and (11) into (7) produces a constitutive function relating the macroscale Green-Lagrange strain and second Piola-Kirchhoff stress tensor of the form

$$\boldsymbol{S}_0 = \hat{\boldsymbol{S}}_0\left(\boldsymbol{E}_0, \boldsymbol{\Xi}_0\right) \tag{12}$$

which is evaluated in five steps:

1. First, the macroscale right stretch tensor $\boldsymbol{U}_0$ is computed from the Green-Lagrange strain $\boldsymbol{E}_0$.
2. Second, the microscale problem with prescribed boundary values given by (8a) is solved.
3. Third, the solution of the microscale problem is postprocessed to obtain the reaction forces.
4. Next, the reaction forces are combined and scaled according to (8b) to produce the homogenized unsymmetric Biot stress tensor $\boldsymbol{B}_0$.
5. Finally, we take the symmetric part of the Biot stress tensor and solve the Lyapunov equation (11) get the homogenized second Piola-Kirchhoff stress tensor $\boldsymbol{S}_0$.

2.3 | Using finite strain three-dimensional material models in membrane elements

The *three-dimensional* constitutive law (12) can be adapted to plane stress (and hence membrane elements) using a variant of the method proposed by Klinkel and Govindjee[1] for using finite strain three-dimensional material models in beam and shell elements. This method involves solving a local nonlinear equation using Newton's method to enforce the plane stress condition. Specifically, the requirement that the out-of-plane components of the second Piola-Kirchhoff stress tensor are zero, i.e.

$$\boldsymbol{S}_0^z = \left[S_0^{(33)}\ S_0^{(13)}\ S_0^{(31)}\right]^T = 0, \tag{13}$$

is enforced by iteratively solving for the corresponding out-of-plane components $\boldsymbol{E}_0^z$ of the Green-Lagrange strain tensor which are treated as unknowns. Each Newton iteration incurs a single evaluation of the three-dimensional constitutive function (12) and its constitutive tangent. Solving the plane stress equation (13) for $\boldsymbol{E}_0^z$ given $\boldsymbol{E}_0^m$, and then evaluating the in-plane components of the second Piola-Kirchhoff stress tensor $\boldsymbol{P}_0^m$ at the resulting configuration corresponds to the evaluation of a plane stress constitutive relation of the form (1) which can be used as a drop-in replacement for a conventional finite strain plane stress constitutive equation. This will be demonstrated in what follows using the general purpose finite element analyzer AERO-S. To complete the description of this multiscale material model we note that for a static analysis or a dynamic analysis using an implicit time-stepping scheme, the consistent constitutive tangent of the plane stress constitutive law is typically required. This quantity, namely $\partial\hat{\boldsymbol{S}}_0^m/\partial\boldsymbol{E}_0^m$ is readily obtained using the constitutive tangent of the three-dimensional constitutive law; the precise definition is given in[1].

2.4 | Discrete governing equations

In this section, the discretized form of the equations governing the multiscale problem of interest are presented, notably including contact at both scales. Specifically,

- At the macroscale we seek the solution of a dynamic contact problem. The deforming bodies are discretized in space using membrane finite elements, and in time using the explicit central difference time-integration scheme. The contact part of the problem is solved using an implicit approach [19].
- At the microscale we seek the solution of static contact problems with nonhomogeneous prescribed boundary displacement and discretized in space using solid finite elements.

With regards to notation, a distinction is made in this work between *unconstrained* degrees of freedom (dofs), i.e., dofs that are not constrained by any essential boundary condition, and *constrained* dofs, i.e., dofs that are constrained by essential boundary conditions. A matrix or vector defined over the set of unconstrained dofs is not designated by any specific symbol. However, a vector of constrained dofs is designated by the ring symbol as in $\mathring{\mathbf{v}}$, and a vector defined over the entire set of constrained and unconstrained dofs is designated by the overline symbol as in $\bar{\mathbf{v}}$. In other words

$$\bar{\mathbf{v}} = \begin{bmatrix} \mathbf{v} \\ \mathring{\mathbf{v}} \end{bmatrix} \tag{14}$$

We assume, without loss of generality, that the discrete form of the macroscale governing equations can be written as a differential-algebraic inequality (DAI):

$$\boldsymbol{M}_0 \ddot{\boldsymbol{u}}_0^{(n+1)} + \boldsymbol{f}_0^{int}\left(\bar{\boldsymbol{u}}_0^{(n+1)}\right) + \boldsymbol{G}_0\left(\bar{\boldsymbol{u}}_0^{(n+2)}\right)\lambda_0^{(n+1)} = \boldsymbol{f}^{ext}\left(t^{(n+1)}\right) \tag{15a}$$

$$\boldsymbol{g}_0\left(\bar{\boldsymbol{u}}_0^{(n+2)}\right) \geq 0 \tag{15b}$$

$$\boldsymbol{\lambda}_0^{(n+1)} \leq 0 \tag{15c}$$

$$\boldsymbol{\lambda}_0^{(n+1)^T}\boldsymbol{g}_0\left(\bar{\boldsymbol{u}}_0^{(n+2)}\right) = 0 \tag{15d}$$

where $\boldsymbol{M}_0$ is the (diagonal) mass matrix, $\boldsymbol{f}_0^{int}$ and $\boldsymbol{f}_0^{ext}$ are the internal and external force vectors, $\boldsymbol{u}_0^{(n+1)}$ and $\ddot{\boldsymbol{u}}_0^{(n+1)}$ are the displacements and accelerations at time $t^{(n+1)}$, $\boldsymbol{g}_0$ is the gap, a vector-valued constraint function representing the discretized non-penetration condition, $\boldsymbol{G}_0$ is the transpose of the constraint Jacobian matrix

$$\boldsymbol{G}_0 = \left[\frac{\partial \boldsymbol{g}_0}{\partial \boldsymbol{u}_0}\right]^T$$

and $\boldsymbol{\lambda}_0^{(n+1)}$ is a vector of Lagrange multipliers at time $t^{(n+1)}$. The dependence of the internal force vector on the history variables is acknowledged but not explicitly stated.

Given some initial values $\boldsymbol{u}_0^{(n)}$, $\dot{\boldsymbol{u}}_0^{(n)}$ and $\ddot{\boldsymbol{u}}_0^{(n)}$ at time $t^{(n)}$, the solution at time $t^{(n+1)}$ is obtained using the following updating procedure:

1. Update displacement
$$\boldsymbol{u}_0^{(n+1)} = \boldsymbol{u}_0^{(n)} + \Delta t_n \dot{\boldsymbol{u}}_0^{(n)} + 0.5\Delta t_n^2 \ddot{\boldsymbol{u}}_0^{(n)}$$
2. Update acceleration and velocity using the predictor-corrector iterative method
   (a) predictor: $k = 0$
$$\begin{aligned}
\ddot{\boldsymbol{u}}_0^{(n+1),0} &= \boldsymbol{M}_0^{-1}\left[\boldsymbol{f}_0^{ext}\left(t^{(n+1)}\right) - \boldsymbol{f}_0^{int}\left(\bar{\boldsymbol{u}}_0^{(n+1)}\right)\right] \\
\dot{\boldsymbol{u}}_0^{(n+1),0} &= \dot{\boldsymbol{u}}_0^{(n)} + 0.5\Delta t_n\left[\ddot{\boldsymbol{u}}_0^{(n)} + \ddot{\boldsymbol{u}}_0^{(n+1),0}\right] \\
\boldsymbol{u}_0^{(n+2),0} &= \boldsymbol{u}_0^{(n+1)} + \Delta t_{n+1}\dot{\boldsymbol{u}}_0^{(n+1),0} + 0.5\Delta t_{n+1}^2 \ddot{\boldsymbol{u}}_0^{(n+1),0}
\end{aligned}$$
   (b) corrector iterations: $k = 1, \ldots$
$$\begin{aligned}
\ddot{\boldsymbol{u}}_0^{(n+1),k} &= \ddot{\boldsymbol{u}}_0^{(n+1),k-1} + \Delta\ddot{\boldsymbol{u}}_0^{(n+1),k} \\
\dot{\boldsymbol{u}}_0^{(n+1),k} &= \dot{\boldsymbol{u}}_0^{(n+1),k-1} + 0.5\Delta t_n \Delta\ddot{\boldsymbol{u}}_0^{(n+1),k} \\
\boldsymbol{u}_0^{(n+2),k} &= \boldsymbol{u}_0^{(n+2),k-1} + 0.5\left[\Delta t_n \Delta t_{n+1} + \Delta t_{n+1}^2\right]\Delta\ddot{\boldsymbol{u}}_0^{(n+1),k}
\end{aligned}$$

At each corrector iteration, the acceleration increment $\Delta\ddot{\boldsymbol{u}}_0^{(n+1),k}$ is obtained by linearizing the gap function $\boldsymbol{g}_0$ and solving the linearized sub-problem

$$\boldsymbol{M}_0\Delta\ddot{\boldsymbol{u}}_0^{(n+1),k} + \boldsymbol{G}_0\left(\bar{\boldsymbol{u}}_0^{(n+2),k-1}\right)\boldsymbol{\lambda}_0^{(n+1),k} = -\tilde{\boldsymbol{f}}_0^{k-1} \tag{16a}$$

$$\boldsymbol{G}_0\left(\bar{\boldsymbol{u}}_0^{(n+2),k-1}\right)^T\Delta\ddot{\boldsymbol{u}}_0^{(n+1),k} \geq -\tilde{\boldsymbol{g}}_0^{k-1} \tag{16b}$$

$$\boldsymbol{\lambda}_0^{(n+1),k} \leq 0 \tag{16c}$$

$$\boldsymbol{\lambda}_0^{(n+1),k\,T}\left[\boldsymbol{G}_0\left(\bar{\boldsymbol{u}}_0^{(n+2),k-1}\right)^T\Delta\ddot{\boldsymbol{u}}_0^{(n+1),k} + \tilde{\boldsymbol{g}}_0^{k-1}\right] = 0 \tag{16d}$$

where:

$$\tilde{\boldsymbol{f}}_0^{k-1} = \boldsymbol{M}_0\left[\ddot{\boldsymbol{u}}_0^{(n+1),k-1} - \ddot{\boldsymbol{u}}_0^{(n+1),0}\right]$$

$$\tilde{\boldsymbol{g}}_0^{k-1} = \frac{2}{\Delta t_n\Delta t_{n+1} + \Delta t_{n+1}^2}\boldsymbol{g}_0\left(\bar{\boldsymbol{u}}_0^{(n+2),k-1}\right)$$

The corrector sub-problem (16) has the form of a quadratic program and can be solved by the primal-dual active set method[20,21]

1. Initialize $\Delta\ddot{\boldsymbol{u}}_0^{(n+1),k}$, $\boldsymbol{\lambda}_0^{(n+1),k}$
2. Iterate
   - Choose active set:
   $$\mathcal{A} = \left\{ i \,:\, \left[\boldsymbol{\lambda}_0^{(n+1),k}\right]_i > 0 \,\wedge\, \left[\boldsymbol{G}_0\left(\bar{\boldsymbol{u}}_0^{(n+2),k-1}\right)\right]_i^T\Delta\ddot{\boldsymbol{u}}_0^{(n+1),k} + \left[\tilde{\boldsymbol{g}}_0^{k-1}\right]_i < 0 \right\}$$
   - Set inactive Lagrange multipliers to zero:
   $$\left[\boldsymbol{\lambda}_0^{(n+1),k}\right]_i = 0 \quad \forall\, i \notin \mathcal{A}$$
   - Solve for $\Delta\ddot{\boldsymbol{u}}_0^{(n+1),k}$ and active Lagrange multipliers:
   $$\boldsymbol{M}_0\Delta\ddot{\boldsymbol{u}}_0^{(n+1),k} + \boldsymbol{G}_0^{\mathcal{A}}\left(\boldsymbol{u}_0^{(n+2),k-1}\right)\boldsymbol{\lambda}_0^{(n+1),\mathcal{A},k} = -\tilde{\boldsymbol{f}}_0^{k-1} \tag{17a}$$
   $$\boldsymbol{G}_0^{\mathcal{A}}\left(\boldsymbol{u}_0^{(n+2),k-1}\right)^T\Delta\ddot{\boldsymbol{u}}_0^{(n+1),k} = -\tilde{\boldsymbol{g}}_0^{\mathcal{A},k-1} \tag{17b}$$
   where the superscript $\mathcal{A}$ applied to a vector indicates its restriction to the active set. Similarly, the superscript $\mathcal{A}$ applied to a matrix indicates its column-wise restriction to the active set.

The active set method sub-problem (17) is a linear saddle-point system. To solve for the active Lagrange multipliers, we first eliminate $\Delta\ddot{\boldsymbol{u}}_0^{(n+1),k}$ and then solve the remaining Schur complement system

$$\left[\boldsymbol{G}_0^{\mathcal{A}\,T}\boldsymbol{M}_0^{-1}\boldsymbol{G}_0^{\mathcal{A}}\right]\boldsymbol{\lambda}_0^{\mathcal{A}} = \tilde{\boldsymbol{g}}_0^{\mathcal{A}} - \boldsymbol{G}_0^{\mathcal{A}\,T}\boldsymbol{M}_0^{-1}\tilde{\boldsymbol{f}}_0. \tag{18}$$

To simplify notation, the superscripts denoting time-step index and predictor-corrector iteration have been omitted here but can be inferred from (17). After solving (18) for the Lagrange multipliers, the acceleration increment can be obtained from (17a).

If $\boldsymbol{G}_0^{\mathcal{A}}$ is rank-deficient then the active set iterations may not converge. In this case, a penalty parameter (μ) can be used to regularize the system, leading to the perturbed systems of the form[22]

$$\left[\boldsymbol{G}_0^{\mathcal{A}\,T}\boldsymbol{M}_0^{-1}\boldsymbol{G}_0^{\mathcal{A}} + \frac{1}{\mu}\boldsymbol{I}\right]\boldsymbol{\lambda}_0^{\mathcal{A}} = \tilde{\boldsymbol{g}}_0^{\mathcal{A}} - \boldsymbol{G}_0^{\mathcal{A}\,T}\boldsymbol{M}_0^{-1}\tilde{\boldsymbol{f}}_0$$

or equivalently,

$$\left[\boldsymbol{M}_0 + \mu\boldsymbol{G}_0^{\mathcal{A}}\boldsymbol{G}_0^{\mathcal{A}\,T}\right]\Delta\ddot{\boldsymbol{u}}_0 = -\tilde{\boldsymbol{f}}_0 - \mu\boldsymbol{G}_0^{\mathcal{A}}\tilde{\boldsymbol{g}}_0^{\mathcal{A}}.$$

This completes the description of the macroscale discrete governing equation and its solution algorithm. Significantly, each time-step incurs only one evaluation of $\boldsymbol{f}^{int}$ which in the context of a multiscale simulation invariably dominates the computational cost of the entire time-step. In order to evaluate this discrete vector of internal forces, the homogenized stress tensor must be computed at each Gauss point of the macroscale finite element model which in turn involves the iterative solution of the Klinkel-Govindjee plane stress equation with one solution of the discrete microscale governing equation required per iteration.

In the presence of contact at the microscale – for example, non-penetration and sliding of yarns in a woven fabric – the discrete form of the microscale governing equation has a similar form to that of the macroscale (15) but without the time-dependence and associated temporal discretization. The external force term is also identically zero and can be omitted; the problem is instead driven by prescribed values of the constrained dofs and can be described as follows

$$\boldsymbol{f}_1^{int}\left(\bar{\boldsymbol{u}}_1\right) + \boldsymbol{G}_1\left(\bar{\boldsymbol{u}}_1\right)\lambda_1 = 0 \tag{19a}$$

$$\boldsymbol{g}_1\left(\bar{\boldsymbol{u}}_1\right) \geq 0 \tag{19b}$$

$$\lambda_1 \leq 0 \tag{19c}$$

$$\lambda_1^T \boldsymbol{g}_1\left(\bar{\boldsymbol{u}}_1\right) = 0 \tag{19d}$$

The quantities $\boldsymbol{F}_1$, $\bar{\boldsymbol{u}}_1$, $\boldsymbol{g}_1$, $\boldsymbol{G}_1$, and λ_1 are all microscale counterparts of the corresponding macroscale quantities defined previously. This problem can be tackled in similar fashion to that of the macroscale by solving a series of linearized sub-problems of the form

$$\boldsymbol{K}_1^{tgt}\Delta\boldsymbol{u}_1^k + \boldsymbol{G}_1\left(\bar{\boldsymbol{u}}_1^{k-1}\right)\lambda_1^k = -\tilde{\boldsymbol{f}}_1^{k-1} \tag{20a}$$

$$\boldsymbol{G}_1\left(\bar{\boldsymbol{u}}_1^{k-1}\right)^T \Delta\boldsymbol{u}_1^k \geq -\tilde{\boldsymbol{g}}_1^{k-1} \tag{20b}$$

$$\lambda_1^k \leq 0 \tag{20c}$$

$$\lambda_1^{kT}\left[\boldsymbol{G}_1\left(\bar{\boldsymbol{u}}_1^{k-1}\right)^T \Delta\boldsymbol{u}_1^k + \tilde{\boldsymbol{g}}_1^{k-1}\right] = 0 \tag{20d}$$

where $\boldsymbol{K}_1^{tgt}$ is the microscale tangent stiffness matrix

$$\boldsymbol{K}_1^{tgt} = \frac{\partial \boldsymbol{f}_1^{int}}{\partial \boldsymbol{u}_1}.$$

Problem (20) can again be solved by the dual-primal active set method proposed for the corresponding macroscale problem (16), although numerous alternatives exist.

The computational homogenization method described in Section 2 provides a very general framework for solving the problem of interest without resorting to any ad-hoc approximation. However, without introducing any further approximation, the framework – although amenable to parallel implementation – is impractical for all but the most modest of applications due to its computational complexity. For example, we estimate that to simulate the inflation of a parachute using a macroscale model comprising 182,554 nodes and 279,025 triangular membrane elements would require 49,604,444,444 constitutive function evaluations and a total run time of approximately 479.95 years for a parallel execution using 96 processing units. Hence, to achieve computational tractability we propose an alternative regression-based surrogate modeling methodology which is described and evaluated in what follows. We emphasize that this methodology relies exclusively on the general framework that has been presented in this section to obtain "training data" that can be used to construct a low-dimensional surrogate model.

3 | REGRESSION-BASED SURROGATE MODEL AT THE MICROSCALE LEVEL

Here, a methodology featuring a regression-based surrogate model is presented for dramatically accelerating the solution of nonlinear dynamic multiscale problems modeled using the multiscale formulation based on the concept of a locally attached microstructure overviewed above. The methodology features a novel training strategy based on the concept of a coupon test analogy. Regression-based surrogate models can be loosely classified as follows:

1. Models whose forms are determined *à-priori* and whose parameters are fitted to available data. Examples of such models are:
   - The St. Venant-Kirchhoff hyperelastic model, a 2-parameter model characterized by a linear relationship between the second Piola-Kirchhoff stress and the Green-Lagrange strain.
   - Hyper-viscoelastic models incorporating a hyperelastic model such as that of St. Venant-Kirchhoff, combined with a viscoelastic component based on a Prony series.
2. Models whose forms are not entirely predetermined but rather discovered at least in part by the regression/fitting process. An example of such a model is an artificial neural network (NN). In this case, certain characteristics of the model may still be specified *à-priori*, such as the number of hidden layers and the functional form of the activation function.

3.1 | Training strategy

A training strategy, i.e., a procedure for sampling the parameter space and collecting stress and strain data is proposed here for constructing the regression-based surrogate models described in this section. For this purpose a model of a small coupon of the macroscale is employed; in this work we utilize a coupon comprising a single membrane element. We emphasize that due to the overwhelming cost of an entire multiscale simulation using a high-dimensional macroscale model, it is not practical to collect data specifically customized to the target application as is sometimes done to train reduced-order models. However, the range of strains to which the coupon model is subject to during the training can be customized to a certain extent for example to target applications with small, medium or large deformations. Due to the small size of the coupon macroscale model, it is feasible to collect data that comprehensively samples in a regular grid the parameter space which is dimension three (recall the microscale prescribed boundary displacements are obtained by a mapping from the in-plane components of the macroscale symmetric Green-Lagrange strain tensor). The macroscale strain can be indirectly specified for the purposes of training by prescribing displacements on the boundary of the macroscale coupon. Figure 3 shows the deformed configurations and corresponding von Mises stress contours for several sampled points in the parameter space obtained during a training performed for the application described in the following section.

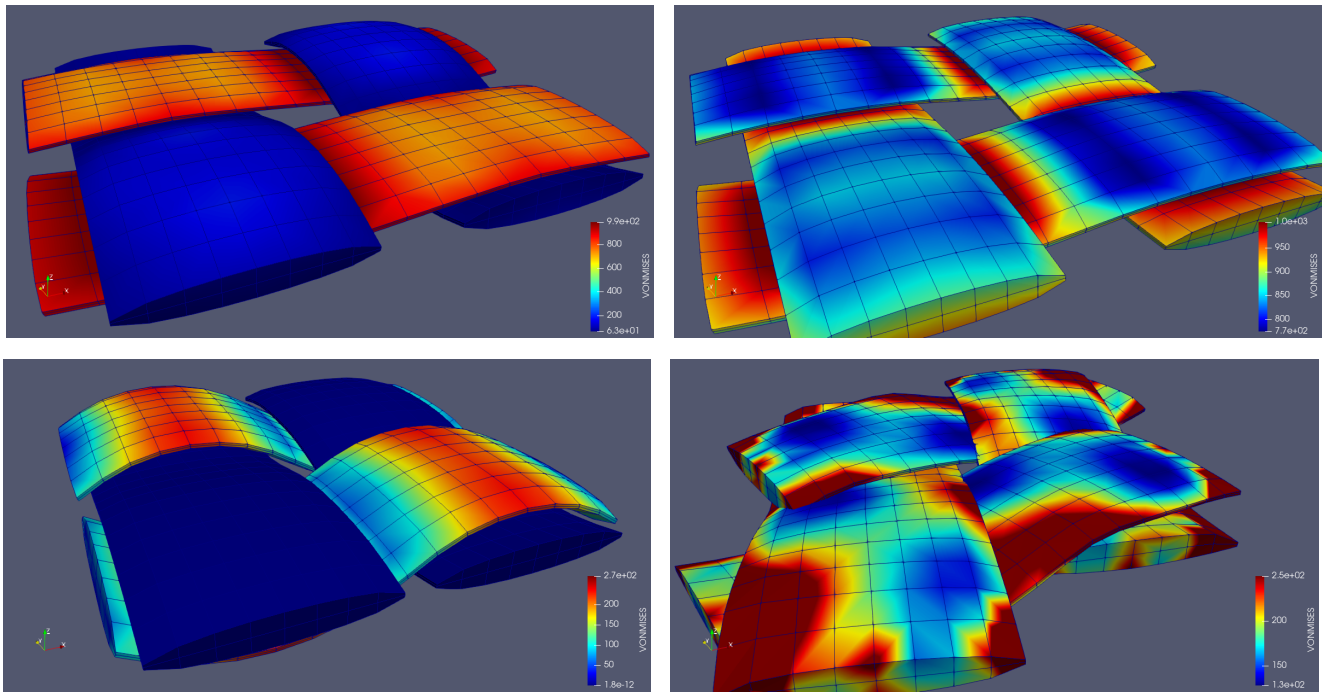

FIGURE 3 Microscale training solution snapshots showing von Mises stress contours for selected points in the sampled parameter space: uniaxial tension (top left), biaxial tension (top right), uniaxial compression (bottom left), and shear (bottom right).

4 | APPLICATIONS

In this section, the following regression-based surrogate microscale models are considered:

- linear

$$\left[S_0^{(11)}\ S_0^{(22)}\ S_0^{(12)}\right]^T = \boldsymbol{C}_1 \left[E_0^{(11)}\ E_0^{(22)}\ 2E_0^{(12)}\right]^T$$

- quadratic

$$\left[S_0^{(11)}\ S_0^{(22)}\ S_0^{(12)}\right]^T = \boldsymbol{C}_2 \left[E_0^{(11)}\ E_0^{(22)}\ 2E_0^{(12)}\ {E_0^{(11)}}^2\ {E_0^{(22)}}^2\ (2E_0^{(12)})^2\ 2E_0^{(12)}E_0^{(22)}\ 2E_0^{(12)}E_0^{(22)}\ E_0^{(11)}E_0^{(22)}\right]^T$$

- neural network (linear model with neural network correction)

$$\left[S_0^{(11)}\ S_0^{(22)}\ S_0^{(12)}\right]^T = \boldsymbol{C}_1 \left[E_0^{(11)}\ E_0^{(22)}\ 2E_0^{(12)}\right]^T + \boldsymbol{N}\left(\left[E_0^{(11)}\ E_0^{(22)}\ 2E_0^{(12)}\right]^T\right)$$

where $\boldsymbol{C}_1 \in \mathbb{R}^{3\times3}$ and $\boldsymbol{C}_2 \in \mathbb{R}^{3\times9}$ are coefficient matrices, and $\boldsymbol{N}$ denotes a fully connected neural network which corrects the linear model by mapping the strain to a stress correction. We will show the proposed neural network model out-performs other surrogate models in terms of the training/test errors. Finally, the neural network model is applied to describe the behavior of a DGB parachute inflation during a supersonic Mars landing event.

4.1 | Training procedures

4.1.1 | Data generation

Strain-stress data pairs $\left(\boldsymbol{E}_0^{(i)}, \boldsymbol{S}_0^{(i)}\right)$, $i = 1, \dots, N$ are generated by performing a numerical coupon test N times, where N is the number of training data points. Each coupon test is depicted in Fig. 4, the right triangle fabric coupon piece is of length 1 m. The displacements of the right angle node and all out-of-plane displacement are constrained to be zero, and prescribed in-plane displacements are applied to the other nodes to generate a specified target strain field. The microscale model (see Section 2.2) is solved at the single Gaussian quadrature point located at the center of the right triangle, which delivers the homogenized strain and stress pairs.

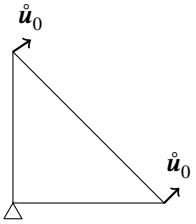

FIGURE 4 Schematic of the coupon test with prescribed displacements (strain fields).

The strain field at the macroscale (fabric coupon) level $\left[E_0^{(11)}\ E_0^{(22)}\ 2E_0^{(12)}\right]^T$ is sampled in a cube of extent $[-0.1, 0.25] \times [-0.1, 0.25] \times [-0.1, 0.25]$. Here, the range of strains is customized to match the application of interest, specifically the inflation of a DGB parachute at typical Mars landing conditions. We sample uniformly in the cube with 17 equidistant points in each component of strain, which accounts for a total of 4913 training data points[1]. Each training data point requires solution of the discrete governing equations (15) governing the multiscale coupon. To facilitate the sampling procedure, each data point is treated as a time-step of a single multiscale simulation in which the prescribed boundary conditions are varied in time along a trajectory (see Figure 5) that traverses all of the data points. Each time-step can be interpreted as an independent static simulation; alternatively each line segment of the trajectory can be interpreted as being associated with the numerical counterpart of a single physical coupon test in which two components of strain are held fixed while the third is varied. Crucially, the converged solution of the microstructure at the previous data point is used as the initial guess for the iterative solution by Newton's method at the subsequent point. In total, the data generation procedure takes about 40 CPU hours. To validate the surrogate models, a further 4913 test data points were generated by shifting the trajectory.

[1]The data is available at https://github.com/Zhengyu-Huang/Fabric-Data.git

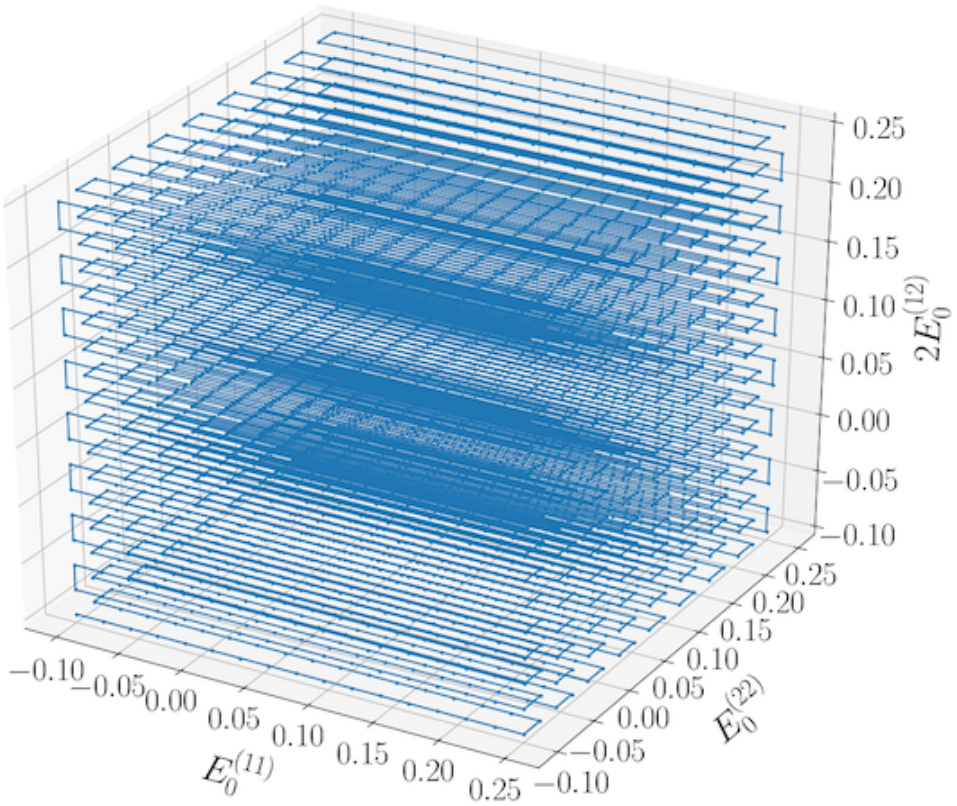

FIGURE 5 Trajectory used for sampling training data points.

4.1.2 | Surrogate model training

The neural network considered in the present work consists of one hidden layer for efficient purpose. Both tanh and ReLU are used as activation functions. The loss function is defined as

$$\sum_{i=1}^{N} ||\boldsymbol{S}_0^{(i)} - \mathcal{M}(\boldsymbol{E}_0^{(i)})||^2 + \lambda||\boldsymbol{\theta}||^2, \tag{21}$$

where $\mathcal{M}$ represents the surrogate model, $\boldsymbol{\theta}$ denotes the hyperparameters in the surrogate model, and L_2 regularization is added with the regularization parameter $\lambda = 10^{-4}$. However, for the fabric material, the shear stress $S_0^{(12)}$ is several magnitudes smaller than the axial stresses $S_0^{(11)}$ and $S_0^{(22)}$ (see Figures 6). To capture the shear effect better, an alternative weighted loss function is also considered

$$\sum_{i=1}^{N} \left(S_0^{(11),(i)} - \mathcal{M}^{(11)}(\boldsymbol{E}_0^{(i)})\right)^2 + \left(S_0^{(22),(i)} - \mathcal{M}^{(22)}(\boldsymbol{E}_0^{(i)})\right)^2 + w^2\left(S_0^{(12),(i)} - \mathcal{M}^{(12)}(\boldsymbol{E}_0^{(i)})\right)^2 + \lambda||\boldsymbol{\theta}||^2, \tag{22}$$

where w is a weighting constant set to 200. In total, six regression-based surrogate models are considered:

- linear model,
- quadratic model,
- NN-tanh model: neural network with six tanh neurons and trained with the unweighted loss function (21),
- NN-ReLU model: neural network with six ReLU neurons and trained with the unweighted loss function (21),
- NN-ReLU model (weighted 6): neural network with six ReLU neurons and trained with the weighted loss function (22), and

- NN-ReLU model (weighted 20): neural network with 20 ReLU neurons and trained with the weighted loss function (22).

Both the linear and quadratic models are trained by least squares without regularization ($\lambda = 0$). All neural network models are trained with the limited-memory BFGS (L-BFGS-B) method[23] with regularization ($\lambda = 10^{-4}$). We use the line search routine in[24], which attempts to enforce the Wolfe conditions[23] by a sequence of polynomial interpolations. Note the BFGS is applicable in our case since the data sets are typically small[25,26]; for large data set the stochastic gradient descent method is suggested.

The total relative training/test errors (excluding the regularization term) and relative errors of each component are reported in Table 1. All neural network models lead to errors one magnitude smaller than the linear or quadratic models. The training/test data and the predictions from all surrogate models are depicted in Figures 6 and 7 for each of the component-wise relations $E_0^{(11)} - S_0^{(11)}$, $E_0^{(22)} - S_0^{(22)}$, and $2E_0^{(12)} - S_0^{(12)}$. The training data shows that the fabric material is flexible with respect to shearing and compression. In particular, the shear stresses are two orders of magnitude smaller than the axial stresses under similar strains. Furthermore, the $E_0^{(11)} - S_0^{(11)}$ and $E_0^{(22)} - S_0^{(22)}$ curves are "flat" when the fabric is compressed; their slopes change suddenly at zero and remain constant in the stretching regime. Due to these features (especially the discontinuity in the slope) in the strain-stress relations, neural network models deliver better approximations and out-perform linear and quadratic regression models. It is worth mentioning the shear stress is small but highly nonlinear. Neural networks trained with the unweighted loss function focus mainly on the axial stresses and fail to capture the nonlinearity in the shear stress (see Figure 6 and Figure 7). By introducing the weighted loss function, the accuracy in the shear stress prediction is improved. Moreover, increasing the number of neurons improves the prediction accuracy (see Table 1). However, it is worth noting that increasing the complexity of the neural network architecture increases computational cost and might lead to over-fitting, especially when the training data is inadequate.

	linear	quadratic	NN-tanh	NN-ReLU	NN-ReLU (weighted 6)	NN-ReLU (weighted 20)
training set	19.5%	10.4%	1.53%	1.57%	2.55%	1.47%
S_{xx}	19.5%	10.4%	1.59%	1.52%	2.55%	1.52%
S_{yy}	19.5%	10.4%	1.48%	1.49%	2.55%	1.42%
S_{xy}	42.4%	38.6%	42.4%	42.4%	27.04%	17.5%
test set	14.0%	9.87%	1.65%	1.60%	2.60%	1.53%
S_{xx}	14.0%	9.87%	1.66%	1.62%	2.60%	1.56%
S_{yy}	14.0%	9.87%	1.64%	1.57%	2.60%	1.50%
S_{xy}	43.0%	34.81%	43.0%	43.0%	26.64%	17.2%

TABLE 1 Total relative error and relative errors of each component of regression-based surrogate models on both training/test data sets.

Regarding the computational cost, the number of operations for a single model evaluation are $O(15)$, $O(51)$, and $O(13 \times \#\text{neurons} + 15)$ for the linear, quadratic, and neural network models, respectively. This indicates that for explicit time-integration schemes whose cost is predominately accounted for by constitutive function evaluations, the simulation cost when a neural network model is utilized can be up to 6 (6 neurons) or 19 (20 neurons) times more expensive than when the linear model is utilized. However, for implicit time-integration schemes, the additional cost incurred by the neural network model would typically be substantially less than for explicit schemes due to the cost of the equation solver which contributes a significant portion of the computational cost regardless of which constitutive model is utilized.

4.2 | Supersonic inflation of a DGB parachute

Finally, the trained NN-ReLU model is applied for describing the canopy behavior in the Fluid-Structure Interaction (FSI) simulation of the inflation dynamics of a DGB parachute system in the low-density, low-pressure, supersonic Martian atmosphere[27,28,29]. While such a simulation is crucial to the understanding of the effects of the fabric material on the performance of the parachute during the deceleration process, its main purpose here is to *validate* the proposed multiscale fabric model using flight data from the landing on Mars of NASA's rover Curiosity.

Component	Parameter	Description	Value
Canopy	D	Diameter	15.447 m
	t	Thickness	7.6×10^{-5} m
	E	*Microscale* yarn Young's modulus	3497 MPa [2]
	ν	*Microscale* yarn Poisson's ratio	0.2
	ρ^C	Density	1154.25 kg m^{-3}
	α	Porosity	0.08
Suspension lines	L	Length	36.56 m
	D	Diameter	3.175×10^{-3} m
	E	Young's modulus	29.5 GPa
	ρ^{SL}	Density	1154.25 kg m^{-3}

TABLE 2 Geometric and material properties of a DGB parachute system[30,27,31].

To this end, the DGB parachute system that successfully deployed in 2012 for the Mars landing of Curiosity is considered (see Figure 8-left). This aerodynamic decelerator system consists of three main components[27]:

- the canopy, which is made of nylon material (see Figure 1),
- the suspension lines, which are made of Technora T221 braided cords, and
- the reentry vehicle.

Its geometric and material properties are listed in Table 2.

The simulation discussed herein starts from the line stretch stage where the suspension line subsystem is deployed but the canopy is folded (see Figure 8-right), and the entire system is prestressed by the folding pattern[29]. The incoming supersonic flow is at the state defined by $M_\infty = 1.8$, $\rho_\infty = 0.0067$ kg m^{-3}, and $p_\infty = 260$ Pa.

Since the Martian atmosphere is mainly composed of carbon dioxide, the viscosity of this gas is modeled using Sutherland's viscosity law with the constant $\mu_0 = 1.57 \times 10^{-6}$ kg m^{-1}s^{-1} and the reference temperature $T_0 = 240$ K. The Reynolds number based on the canopy diameter is 4.06×10^6. Hence, the flow is assumed to have transitioned to the turbulent regime, which is modeled here using Vreman's eddy viscosity subgrid-scale model for turbulent shear flow[32] with model constant $C_s = 0.07$.

The in-house Eulerian computational framework with an immersed (embedded) boundary method — Finite Volume method with Exact two-phase or two-material Riemann problems (FIVER)[33,34,35,36,28] is adopted in the present work, due to the large deformation of the parachute system. This method has previously been successfully employed for the simulation of the failure analysis of submerged structures subjected to explosions and implosions[37]. It incorporates in the framework a parallel Adaptive Mesh Refinement (AMR) based on newest vertex bisection[38,39], which enables the capturing of various interactions between the fluid subsystem, the nonlinear parachute subsystem, and the forebody.

The canopy of the DGB parachute consists of band and disk gores. Here, these are discretized by 279,025 geometrically nonlinear membrane elements. The suspension line subsystem contains 80 lines, each of which is discretized by 500 geometrically nonlinear beam elements. The reentry vehicle, it is modeled as a fixed rigid body that is embedded, together with the entire aerodynamic decelerator system, in the embedding computational fluid domain (see Figure 8).

The aforementioned computational fluid domain is a box of size 200 m × 160 m × 160 m. It is initially discretized by a mesh comprising 2,778,867 nodes and 16,308,672 tetrahedra. During the FSI simulation reported below, AMR is applied to track and resolve the boundary layer and flow features. The specified characteristic mesh sizes near the reentry vehicle and canopy are 2.5 cm and 5 cm, respectively. The specified characteristic mesh size in the wake and near the shock is 10 cm.

Since the canopy is made of nylon fabric with an 8% void fraction, its permeability is modeled using an homogenized porous wall model[40,41]. Due to the massive self-contact of the parachute canopy during its dynamic inflation, the explicit central difference time-integration scheme is used to advance in time the semi-discrete state of the structural subsystem. A small amount of Rayleigh damping is applied to stabilize the system.

[2]The microscale yarn Young's modulus is roughly estimated from the Young's modulus of the macroscale nylon.

	Number of cores	Wall-clock time (h)
Training data generation	1	40
Training	1	0.01
Fluid solver	480	96.14
NN-ReLU structure solver	96	19.52
NN-ReLU (weighted 20) structure solver	96	24.82
St. Venant-Kirchhoff structure solver	96	2.96
FE^2-based structure solver	96	4204336.55[3]

TABLE 3 Computational costs of each component in the proposed framework for the parachute inflation dynamics simulation.

First, a quasi-steady state of the flow past the folded parachute configuration shown in Figure 8-right is computed assuming that this configuration is rigid and fixed. Using this CFD solution and the aforementioned prestressed state of the structural model of the parachute system as initial fluid and structural conditions, respectively, the FSI simulation of the inflation dynamics of the DGB parachute is performed in the time-interval $[0, 0.8]$ s. The length of this time-interval is such that it covers the inflation process as well as a few breathing cycles of the DGB parachute system. As stated above, the explicit central difference time-integrator is applied to advancing in time the semi-discrete structural subsystem. On the other hand, the implicit, 3-point BDF scheme is applied to time-integrate the semi-discrete fluid state. The fluid and structural discretizations are coupled for this simulation using the stability-preserving, second-order, time-accurate, implicit-explicit fluid-structure staggered solution procedure presented in[42]. The fluid-structure coupling time-step is set to $\Delta t_{F/S} = 10^{-5}$ s.

Figure 9 graphically depicts the time-evolutions of the dynamic inflation of the DGB parachute and the flow Mach number around it. The parachute is fully inflated at approximately $t = 0.24$ s; after this time, it starts the breathing cycles expected from a violent, high-speed, dynamic, inflation process.

Figure 10 reports the time-histories of the total drag force predicted by the FSI simulation described above. For reference, this figure also includes the time-history of the total drag generated by the parachute system of NASA's rover Curiosity as measured during Mars landing[27], and the simulation with the classical St. Venant-Kirchhoff model in[29]. The NN-ReLU models deliver a stable result, which is in reasonably good agreement with the experimental data. However, the effects of the constitutive relations of the nylon fabric is rather weak in terms of the drag performance. Figure 11 reports the time-histories of the maximum von Mises stresses, an indicator of material failure, predicted by the FSI simulation described above. The results delivered by NN-ReLU model and NN-ReLU (weighted 20) model, which is trained with the weighted loss function are similar. And this indicates the shear effect of the nylon fabric is not significant during the inflation. However the comparison with the result delivered by St. Venant-Kirchhoff model illustrates that flexibility with respect to shearing and compression in the multiscale fabric model leads to lower von Mises stresses in the parachute "breathing" cycle after the full inflation. This disparity is also shown in Fig. 12, which depicts the time-evolutions of the von Mises stress fields. Although further (experimental) investigation is required to conclude which model is more reliable, this comparison illustrates the potential of multiscale constitutive model for improving the prediction of material failure.

The computational costs of each component, including both the training procedure and the FSI simulation, are reported in Table 3. It is worth mentioning the the estimated simulation time for the direct FE^2 simulation is also reported in Table 3, and the speedup of the NN-based surrogate model based on this estimation is about 7×10^4 (with training costs included). This demonstrates the strength of NN-based surrogate in the constitutive modeling.

[3]The wall-clock time is estimated as the multiplication of the number of FE^2 model evaluations on each CPU and the cost of a single evaluation.

5 | CONCLUSIONS

A general framework has recently been developed for computationally tractable, nonlinear multiscale modeling of membrane fabrics. It is enabled by the coherent utilization of several established methodologies

- computational homogenization known as Finite Element squared or FE^2 based on the concept of a locally attached microstructure,
- numerical enforcement of the membraneâĂŹs plane stress condition, and
- regression; a surrogate constitutive model is "discovered" using data generated by many multiscale numerical simulations of a small fabric coupon.

This framework encompasses a cascade of multiscale models ranging from the highest fidelity (without surrogate) to the lowest (linear regression surrogate) and has been demonstrated on the simulation of inflation of a disk-gap-band parachute in supersonic Martian atmospheric entry conditions. In this demonstration, the utilization of a neural network surrogate was able to achieve speedups of approximately 7×10^4 relative to the highest fidelity, at an overall cost within one order of magnitude of a conventional (i.e. linear elastic model) material. The proposed discovery of a surrogate constitutive model by means of numerical coupon testing is analogous to the experimental testing procedure used to identify the parameters (e.g. the YoungâĂŹs modulus) of conventional material models. A highlight of the proposed framework is that while experimental data is typically limited to uniaxial tension (occasionally biaxial and/or shear data may also be available), numerical data suffers from no such limitation and we can readily explore the entire parameter space (i.e. all physically admissible combinations of normal and shear strains) during the discovery in order to characterize complex and unconventional materials. However, the generation of training data can be a substantial cost. We propose an application of model-order reduction (see Appendix A) using a novel in-situ training approach to accelerate this task; this will be the topic of a companion paper[43].

ACKNOWLEDGMENTS

Philip Avery, Daniel Z. Huang, Johanna Ehlers and Charbel Farhat acknowledge partial support by the Jet Propulsion Laboratory (JPL) under Contract JPL-RSA No. 1590208, and partial support by the National Aeronautics and Space Administration (NASA) under Early Stage Innovations (ESI) Grant NASA-NNX17AD02G. Parts of this work were completed at the JPL, California Institute of Technology, under a contract with NASA. Optical microscope photographs were taken by Cheyenne Hua at the JPL. Any opinions, findings, and conclusions or recommendations expressed in this paper are those of the authors and do not necessarily reflect the views of JPL or NASA.

APPENDIX

A PROJECTION-BASED REDUCED ORDER SURROGATE MICROSCALE MODEL

Here, a reduction/hyperreduction framework is presented for dramatically accelerating the solution of nonlinear dynamic multiscale problems modeled using the multiscale formulation based on the concept of a locally attached microstructure overviewed above. This framework constitutes a generalization of Zahr[2] to include

- a treatment of contact based on the method originally proposed in[44] and featuring the application of a non-negative matrix factorization scheme to the construction of a positive reduced-order basis for the contact forces, and
- a novel training strategy based on the concept of a coupon test analogy.

Unlike in[2] where reduction was considered at all scales, we will restrict the exposition here to reduction of the microscale only. Specifically, the Proper Orthogonal Decomposition (POD) method is used to construct a PROM at the microscale, and a

computational approach based on the Energy Conserving Sampling and Weighting (ECSW) method[45,46] is used to hyperreduce it. Training is performed offline (i.e. *à-priori*) using a small multiscale coupon model.

A.1 Reduction of the primal unknowns

At the microscale (scale 1), the number of primal dofs n_1 of the computational model is reduced by searching for the primal solution $\boldsymbol{u}_1$ of the problem of interest in a carefully constructed low-dimensional subspace, i.e.,

$$\boldsymbol{u}_1 \approx \boldsymbol{V}_1 \boldsymbol{y}_1 \tag{A1}$$

where $\boldsymbol{V}_1 \in \mathbb{R}^{n_1 \times r_1}$ is a Reduced Order Basis (ROB) representing a low-dimensional subspace, $\boldsymbol{y}_1 \in \mathbb{R}^{r_1}$ is the vector of generalized coordinates of $\boldsymbol{u}_1$ in this basis, and $r_1 \ll n_1$. The ROB is chosen to be orthonormal with respect to the identity matrix, i.e.,

$$\boldsymbol{V}_1^T \boldsymbol{V}_1 = \boldsymbol{I}.$$

In this work, the ROB is constructed using POD and the method of snapshots[47]. To this effect, let $\{\boldsymbol{u}_1^{(1)}, \dots, \boldsymbol{u}_1^{(m_1)}\}$ be m_1 state snapshots at scale 1, i.e., solutions of (19) for different prescribed boundary displacements. We define the *primal* snapshot matrix $\boldsymbol{Y}_1^u$ as the $n_1 \times m_1$ matrix whose columns are comprised of the snapshots

$$\boldsymbol{Y}_1^u = \left[\boldsymbol{u}_1^{(1)} \ \cdots \ \boldsymbol{u}_1^{(m_1)}\right].$$

The ROB $\boldsymbol{V}_1$ is composed of the first r_1 principle components, or left singular vectors of $\boldsymbol{Y}_1^u$.

Furthermore, it follows from (2) that the microscale constrained dofs' displacement $\mathring{\boldsymbol{u}}_1$ also lies in a low dimensional subspace associated with a vector of generalized coordinates identified as the column-wise vectorization of the right stretch strain tensor $\boldsymbol{U}_0 - \boldsymbol{I}$, i.e.

$$\mathring{\boldsymbol{u}}_1 = \boldsymbol{\Pi}_1 \begin{bmatrix} \mathring{\boldsymbol{X}}_1 & 0 & 0 \\ 0 & \mathring{\boldsymbol{X}}_1 & 0 \\ 0 & 0 & \mathring{\boldsymbol{X}} \end{bmatrix} \mathrm{vec}\left(\boldsymbol{U}_0 - \boldsymbol{I}\right) \quad = \mathring{\boldsymbol{V}}_1 \mathring{\boldsymbol{y}}_1 \tag{A2}$$

where $\boldsymbol{\Pi}_1$ is a permutation matrix and $\mathring{\boldsymbol{X}}_1$ is a matrix whose three columns represent the x, y, and z nodal coordinates, respectively, of the constrained nodes on the microscale boundary. The definition of $\bar{\boldsymbol{y}}_1$ follows from to the notational convention (14); similarly a basis encompassing both unconstrained and constrained dofs can be represented, up to a permutation, as

$$\bar{\boldsymbol{V}}_1 = \begin{bmatrix} \boldsymbol{V}_1 & 0 \\ 0 & \mathring{\boldsymbol{V}}_1 \end{bmatrix}.$$

The dimensionality of the discrete governing equations (19) is reduced at scale 1 by performing a Galerkin projection, i.e., substituting (A1) in these equations and projecting the first of them onto the column space of $\boldsymbol{V}_1$. This leads to the PROM

$$\boldsymbol{V}_1^T \boldsymbol{f}_1^{int}\left(\bar{\boldsymbol{V}}_1 \bar{\boldsymbol{y}}_1\right) + \boldsymbol{V}_1^T \boldsymbol{G}_1\left(\bar{\boldsymbol{V}}_1 \bar{\boldsymbol{y}}_1\right) \lambda_1 = 0 \tag{A3a}$$

$$\boldsymbol{g}_1\left(\bar{\boldsymbol{V}}_1 \bar{\boldsymbol{y}}_1\right) \geq 0 \tag{A3b}$$

$$\lambda_1 \leq 0 \tag{A3c}$$

$$\lambda_1^T \boldsymbol{g}_1\left(\bar{\boldsymbol{V}}_1 \bar{\boldsymbol{y}}_1\right) = 0 \tag{A3d}$$

Despite the fact that the equations (A3) are characterized by a reduced dimensionality, their solution remains computationally intensive due to the presence of the nonlinear term $\boldsymbol{f}_1^{int}$. Indeed, the projection of this term implies that every evaluation of $\boldsymbol{V}_1^T \boldsymbol{f}_1^{int}$ requires the reconstruction of the full state using the approximation $\bar{\boldsymbol{V}}_1 \bar{\boldsymbol{y}}_1$, the integration and assembly of the internal force vector over the entire computational mesh, and its projection onto the subspace represented by the ROB $\boldsymbol{V}_1$. Because such computations scale with the size n_1 of the high-dimensional model at level 1, they cannot be performed using limited resources or at low computational cost, and much less in real time. Hence, they constitute a substantial bottleneck in the solution of (A3). For this reason, a number of hyperreduction methods have been proposed to overcome this bottleneck introduced by nonlinear terms. For solid mechanics and structural dynamics problems, the ECSW method is our preferred hyperreduction method due to its desirable structure-preserving and numerical stability properties[46]. However, in principle, any other hyperreduction method can be used to overcome the aforementioned computational bottleneck.

As introduced in[45], the ECSW method amounts to a "mesh reduction" algorithm which samples a set of elements $\mathscr{V}_1' \subset \mathscr{V}_1$ and attributes to each sampled element e a positive weight $\alpha_1^e > 0$ such that

$$\begin{aligned}\bar{\boldsymbol{V}}_1^T \bar{\boldsymbol{f}}_1^{int}\left(\bar{\boldsymbol{V}}_1 \bar{\boldsymbol{y}}_1\right) &= \sum_{e\in\mathscr{V}_1} \left(\bar{\boldsymbol{V}}_1^e\right)^T \bar{\boldsymbol{f}}_1^{int^e}\left(\bar{\boldsymbol{V}}_1^e \bar{\boldsymbol{y}}_1\right) \\ &\approx \sum_{e\in\mathscr{V}_1'} \alpha_1^e \left(\bar{\boldsymbol{V}}_1^e\right)^T \bar{\boldsymbol{f}}_1^{int^e}\left(\bar{\boldsymbol{V}}_1^e \bar{\boldsymbol{y}}_1\right) \quad = \bar{\boldsymbol{f}}_{1_r}^{int}\left(\bar{\boldsymbol{y}}_1\right)\end{aligned} \tag{A4}$$

In the above expressions, the superscript e designates the *restriction* of a global vector or matrix to element e, and the so-called reduced mesh $|\mathscr{V}_1'| \ll |\mathscr{V}_1|$ can be computed using Lawson and Hanson's Non-Negative Least Squares (NNLS) algorithm[48] or alternative L1 minimization algorithms[49] in a training step that seeks to minimize the size of the reduced mesh while maintaining an acceptable approximation error for the ensemble of the training data.

In addition to achieving scalability with respect to the size n_1 of the PROM only in the computation of the components of the internal force vector corresponding to unconstrained dofs, the reduced mesh ensures that scale transmission is performed efficiently, i.e., without any operation whose computational complexity scales with $|\mathscr{V}_1|$. This is evident in the transmission to finer scales where $\mathring{\boldsymbol{u}}_1^e$ is required for each $e \in \mathscr{S}_1'$ while with regards to transmission to coarser scales, the homogenized macroscopic unsymmetric Biot stress tensor is approximated as

$$\mathrm{vec}(\boldsymbol{B}_0) \approx \frac{1}{|\mathscr{B}_1|}\mathring{\boldsymbol{f}}_{1_r}\left(\bar{\boldsymbol{y}}_1\right)$$

where $\mathscr{S}_1' \subset \mathscr{S}_1$ denotes the subset of surface elements contained in the reduced mesh $\mathscr{V}_1'$, and $\mathring{\boldsymbol{f}}_{1_r}$ in general is the restriction of the *total* vector of reduced forces – both internal and contact – to the constrained generalized coordinates, i.e.

$$\mathring{\boldsymbol{f}}_{1_r} = \mathring{\boldsymbol{f}}_{1_r}^{int}\left(\bar{\boldsymbol{y}}_1\right) + \mathring{\boldsymbol{V}}_1^T \mathring{\boldsymbol{G}}_1\left(\bar{\boldsymbol{V}}_1 \bar{\boldsymbol{y}}_1\right)\lambda_1$$

although the microscale mesh can in some cases be constructed in such a way that the contact forces will contribute nothing to this quantity. This requires a separation of at least one element between the contact surface and the boundary to be maintained.

A.2 Reduction of the dual unknowns

At the microscale (scale 1), the number of dual dofs n_1^λ of the computational model can also be reduced by searching for the dual solution λ_1 of the problem of interest in another carefully constructed low-dimensional subspace, i.e.,

$$\lambda_1 \approx \boldsymbol{W}_1 \boldsymbol{z}_1 \tag{A5}$$

where $\boldsymbol{W}_1 \in \mathbb{R}^{n_1^\lambda \times r_1^\lambda}$ is a dual reduced order basis representing a low-dimensional subspace, $\boldsymbol{z}_1 \in \mathbb{R}^{r_1^\lambda}$ is the vector of generalized coordinates of λ_1 in this basis, and $r_1^\lambda \ll n_1^\lambda$. The dual ROB is chosen such that it has no negative elements.

In this work, the dual ROB is constructed using Non-negative Matrix Factorization (NMF). To this effect, let $\{\lambda_1^{(1)}, \ldots, \lambda_1^{(m_1)}\}$ be m_1 state snapshots at scale 1, i.e., solutions of (19) for different prescribed boundary displacements. We define the *dual* snapshot matrix $\boldsymbol{Y}_1^\lambda$ as the $n_1^\lambda \times m_1$ matrix whose columns are comprised of the snapshots

$$\boldsymbol{Y}_1^\lambda = \left[\lambda_1^{(1)} \ \cdots \ \lambda_1^{(m_k)}\right]$$

The dual ROB $\boldsymbol{W}_1$ is composed of the columns of the left factor of the NMF of $\boldsymbol{Y}_k^\lambda$[44].

The dimensionality of the reduced governing equations (A3) is further reduced at scale 1 by substituting (A5) and projecting the gap function $\boldsymbol{g}_1$ onto the column space of $\boldsymbol{W}_1$. Hyperreduction of the internal force is also accounted for. This leads to the PROM

$$\boldsymbol{f}_{1_r}^{int}\left(\bar{\boldsymbol{y}}_1\right) + \boldsymbol{V}_1^T \boldsymbol{G}_1\left(\bar{\boldsymbol{V}}_1 \bar{\boldsymbol{y}}_1\right)\boldsymbol{W}_1 \boldsymbol{z}_1 = 0 \tag{A6a}$$

$$\boldsymbol{W}_1^T \boldsymbol{g}_1\left(\bar{\boldsymbol{V}}_1 \bar{\boldsymbol{y}}_1\right) \geq 0 \tag{A6b}$$

$$\boldsymbol{z}_1 \leq 0 \tag{A6c}$$

$$\boldsymbol{z}_1^T \boldsymbol{W}_1^T \boldsymbol{g}_1\left(\bar{\boldsymbol{V}}_1 \bar{\boldsymbol{y}}_1\right) = 0 \tag{A6d}$$

Typically, the evaluation of the gap function and its Jacobian does not require a reconstruction of the full state but only its restriction to the contact surface. Furthermore, Galerkin projection of the contact force term can be optimized by accounting for the sparsity of the Jacobian. Specifically, only the row-wise restriction of $\boldsymbol{G}_1$ to the contact surface is non-zero. Nevertheless,

these evaluations may still incur a substantial computational cost. In principal, hyperreduction can be applied to further accelerate the evaluation of the reduced gap function and its Jacobian. This is an active topic of research but is not employed in the present work. However, we note that in the case of linear constraints the proposed reduction of the dual variables leads to terms involving reduced-order matrices that are *precomputable*, and as such does not generate any bottleneck in the online solution of the reduced-order discrete microscale equations. Consequently, just like in the case of any other linear terms, their efficient processing does not require any hyperreduction.

References

1. Klinkel S, Govindjee S. Using finite strain 3D-material models in beam and shell elements. *Engineering Computations* 2002; 19(3): 254–271.
2. Zahr MJ, Avery P, Farhat C. A multilevel projection-based model order reduction framework for nonlinear dynamic multiscale problems in structural and solid mechanics. *International Journal for Numerical Methods in Engineering* 2017; 112(8): 855–881.
3. Yvonnet J, He QC. The reduced model multiscale method (R3M) for the non-linear homogenization of hyperelastic media at finite strains. *Journal of Computational Physics* 2007; 223(1): 341–368.
4. Knap J, Barton N, Hornung R, Arsenlis A, Becker R, Jefferson D. Adaptive sampling in hierarchical simulation. *International journal for numerical methods in engineering* 2008; 76(4): 572–600.
5. Le B, Yvonnet J, He QC. Computational homogenization of nonlinear elastic materials using neural networks. *International Journal for Numerical Methods in Engineering* 2015; 104(12): 1061–1084.
6. Lu X, Giovanis DG, Yvonnet J, Papadopoulos V, Detrez F, Bai J. A data-driven computational homogenization method based on neural networks for the nonlinear anisotropic electrical response of graphene/polymer nanocomposites. *Computational Mechanics* 2019; 64(2): 307–321.
7. Coenen E, Kouznetsova V, Geers M. Computational homogenization for heterogeneous thin sheets. *International Journal for Numerical Methods in Engineering* 2010; 83(8-9): 1180–1205.
8. Ha-Minh C, Kanit T, Boussu F, Imad A. Numerical multi-scale modeling for textile woven fabric against ballistic impact. *Computational Materials Science* 2011; 50(7): 2172–2184.
9. Larsson R, Landervik M. A stress-resultant shell theory based on multiscale homogenization. *Computer Methods in Applied Mechanics and Engineering* 2013; 263: 1–11.
10. Miehe C, Schröder J, Schotte J. Computational homogenization analysis in finite plasticity simulation of texture development in polycrystalline materials. *Computer methods in applied mechanics and engineering* 1999; 171(3-4): 387–418.
11. Simo J, Govindjee S. Exact closed-form solution of the return mapping algorithm in plane stress elasto-viscoplasticity. *Engineering Computations* 1988; 5(3): 254–258.
12. Smit R, Brekelmans W, Meijer H. Prediction of the mechanical behavior of nonlinear heterogeneous systems by multi-level finite element modeling. *Computer methods in applied mechanics and engineering* 1998; 155(1-2): 181–192.
13. Feyel F, Chaboche JL. FE2 multiscale approach for modelling the elastoviscoplastic behaviour of long fibre SiC/Ti composite materials. *Computer methods in applied mechanics and engineering* 2000; 183(3-4): 309–330.
14. Kouznetsova V, Brekelmans W, Baaijens F. An approach to micro-macro modeling of heterogeneous materials. *Computational mechanics* 2001; 27(1): 37–48.
15. Melbø H, Kvamsdal T. Goal oriented error estimators for Stokes equations based on variationally consistent postprocessing. *Computer methods in applied mechanics and engineering* 2003; 192(5-6): 613–633.
16. Ciarlet PG. *Mathematical Elasticity: Volume I: three-dimensional elasticity*. North-Holland . 1988.

17. Yvonnet J, Monteiro E, He QC. Computational homogenization method and reduced database model for hyperelastic heterogeneous structures. *International Journal for Multiscale Computational Engineering* 2013; 11(3).

18. Ogden RW. Nonlinear elasticity, anisotropy, material stability and residual stresses in soft tissue. In: Springer. 2003 (pp. 65–108).

19. Salveson MW, Taylor RL. Solution of dynamic contact problems by implicit/explicit methods. *Rept. UCRL-CR-125780, Lawrence Livermore National Laboratory, Livermore, CA* 1996.

20. Hintermüller M, Ito K, Kunisch K. The primal-dual active set strategy as a semismooth Newton method. *SIAM Journal on Optimization* 2002; 13(3): 865–888.

21. Hüeber S, Wohlmuth BI. A primal–dual active set strategy for non-linear multibody contact problems. *Computer Methods in Applied Mechanics and Engineering* 2005; 194(27-29): 3147–3166.

22. Hintermüller M, Kunisch K. Path-following methods for a class of constrained minimization problems in function space. *SIAM Journal on Optimization* 2006; 17(1): 159–187.

23. Byrd RH, Lu P, Nocedal J, Zhu C. A limited memory algorithm for bound constrained optimization. *SIAM Journal on scientific computing* 1995; 16(5): 1190–1208.

24. Moré JJ, Thuente DJ. Line search algorithms with guaranteed sufficient decrease. *ACM Transactions on Mathematical Software (TOMS)* 1994; 20(3): 286–307.

25. Huang DZ, Xu K, Farhat C, Darve E. Predictive modeling with learned constitutive laws from indirect observations. *arXiv preprint arXiv:1905.12530* 2019.

26. Xu K, Huang DZ, Darve E. Learning constitutive relations using symmetric positive definite neural networks. *arXiv preprint arXiv:2004.00265* 2020.

27. Cruz JR, Way DW, Shidner JD, Davis JL, Adams DS, Kipp DM. Reconstruction of the Mars science laboratory parachute performance. *Journal of Spacecraft and Rockets* 2014; 51(4): 1185–1196.

28. Huang DZ, Avery P, Farhat C. An embedded boundary approach for resolving the contribution of cable subsystems to fully coupled fluid-structure Interaction. *arXiv preprint arXiv:1908.08382* 2019.

29. Huang DZ, Avery P, Farhat C, Rabinovitch J, Derkevorkian A, Peterson LD. Modeling, simulation and validation of supersonic parachute inflation dynamics during Mars landing. In: American Institute of Aeronautics and Astronautics. ; 2020: 0313.

30. Lin JK, Shook LS, Ware JS, Welch JV. Flexible material systems testing. NASA Report CR-2010-216854; 2010.

31. Hill JL. *Mechanical property determination for flexible material systems*. PhD thesis. Georgia Institute of Technology, North Ave NW, Atlanta, GA 30332; 2016.

32. Vreman A. An eddy-viscosity subgrid-scale model for turbulent shear flow: Algebraic theory and applications. *Physics of fluids* 2004; 16(10): 3670–3681.

33. Wang K, Rallu A, Gerbeau JF, Farhat C. Algorithms for interface treatment and load computation in embedded boundary methods for fluid and fluid–structure interaction problems. *International Journal for Numerical Methods in Fluids* 2011; 67(9): 1175–1206.

34. Farhat C, Gerbeau JF, Rallu A. FIVER: A finite volume method based on exact two-phase Riemann problems and sparse grids for multi-material flows with large density jumps. *Journal of Computational Physics* 2012; 231(19): 6360–6379.

35. Lakshminarayan V, Farhat C, Main A. An embedded boundary framework for compressible turbulent flow and fluid–structure computations on structured and unstructured grids. *International Journal for Numerical Methods in Fluids* 2014; 76(6): 366–395.

36. Main A, Zeng X, Avery P, Farhat C. An enhanced FIVER method for multi-material flow problems with second-order convergence rate. *Journal of Computational Physics* 2017; 329: 141–172.

37. Wang K, Lea P, Farhat C. A computational framework for the simulation of high-speed multi-material fluid–structure interaction problems with dynamic fracture. *International Journal for Numerical Methods in Engineering* 2015; 104(7): 585–623.

38. Mitchell WF. *Unified multilevel adaptive finite element methods for elliptic problems*. PhD thesis. University of Illinois at Urbana-Champaign, ; 1988.

39. Borker R, Huang D, Grimberg S, Farhat C, Avery P, Rabinovitch J. Mesh adaptation framework for embedded boundary methods for computational fluid dynamics and fluid-structure interaction. *International Journal for Numerical Methods in Fluids* 2019.

40. Huang DZ, Wong ML, Lele SK, Farhat C. A homogenized flux-body force approach for modeling porous wall boundary conditions in compressible viscous flows. *arXiv preprint arXiv:1907.09632* 2019.

41. Huang Z, Avery P, Farhat C, Rabinovitch J, Derkevorkian A, Peterson LD. Simulation of parachute inflation dynamics using an Eulerian computational framework for fluid-structure interfaces evolving in high-speed turbulent flows. In: AIAA. ; 2018: 1540.

42. Farhat C, Rallu A, Wang K, Belytschko T. Robust and provably second-order explicit–explicit and implicit–explicit staggered time-integrators for highly non-linear compressible fluid–structure interaction problems. *International Journal for Numerical Methods in Engineering* 2010; 84(1): 73–107.

43. He W, Avery P, Farhat C. In-situ adaptive reduction of nonlinear multiscale structural dynamics models. *arXiv preprint arXiv:2004.00153* 2020.

44. Balajewicz M, Amsallem D, Farhat C. Projection-based model reduction for contact problems. *International Journal for Numerical Methods in Engineering* 2016; 106(8): 644–663.

45. Farhat C, Avery P, Chapman T, Cortial J. Dimensional reduction of nonlinear finite element dynamic models with finite rotations and energy-based mesh sampling and weighting for computational efficiency. *International Journal for Numerical Methods in Engineering* 2014; 98(9): 625–662.

46. Farhat C, Chapman T, Avery P. Structure-preserving, stability, and accuracy properties of the energy-conserving sampling and weighting method for the hyper reduction of nonlinear finite element dynamic models. *International Journal for Numerical Methods in Engineering* 2015; 102(5): 1077–1110.

47. Sirovich L. Turbulence and the dynamics of coherent structures. I. Coherent structures. *Quarterly of applied mathematics* 1987; 45(3): 561–571.

48. Lawson CL, Hanson RJ. *Solving least squares problems*. 15. Siam . 1995.

49. Chapman T, Avery P, Collins P, Farhat C. Accelerated mesh sampling for the hyper reduction of nonlinear computational models. *International Journal for Numerical Methods in Engineering* 2017; 109(12): 1623–1654.

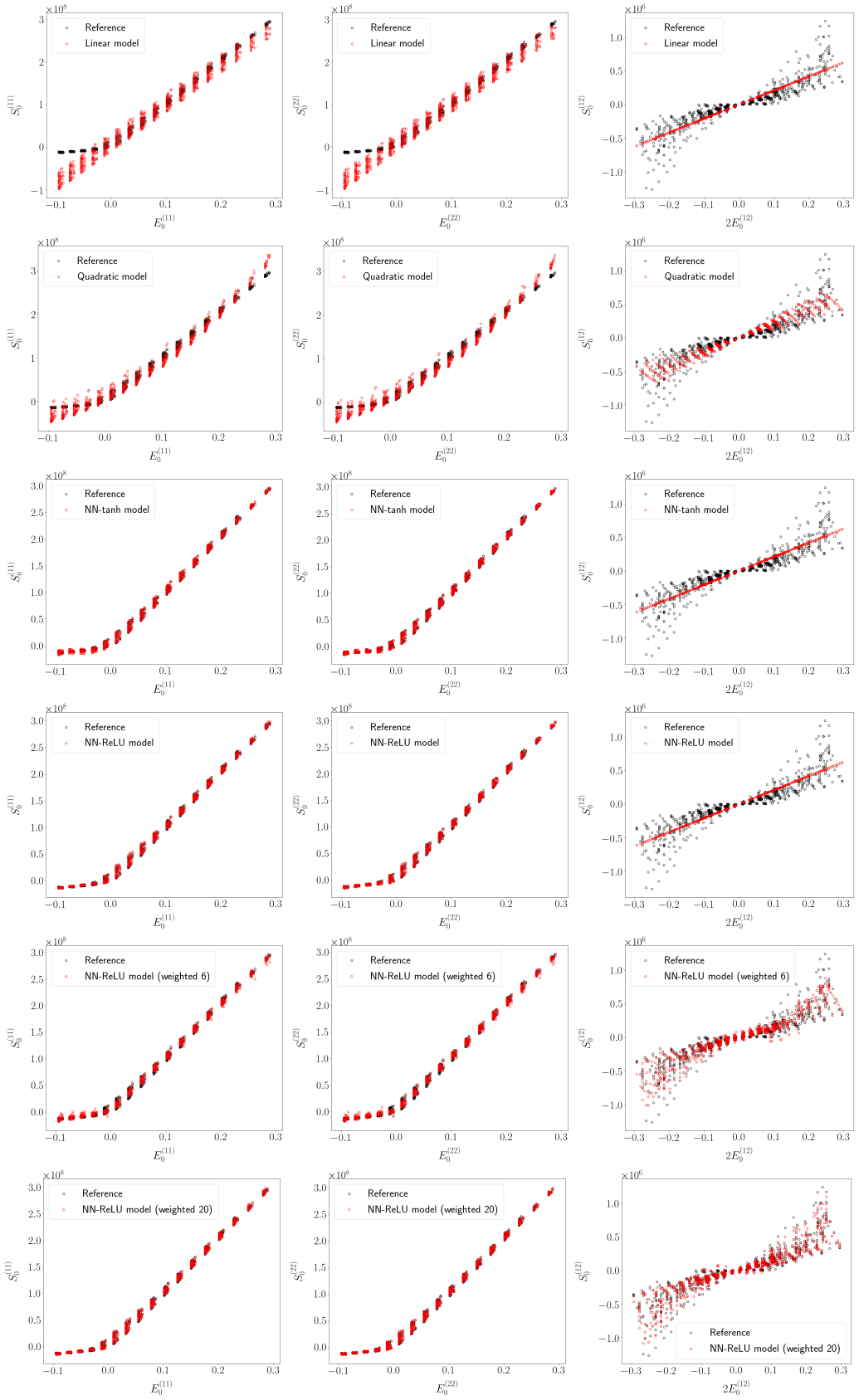

FIGURE 6 Reference and predicted strain-stress pairs for the training data set.

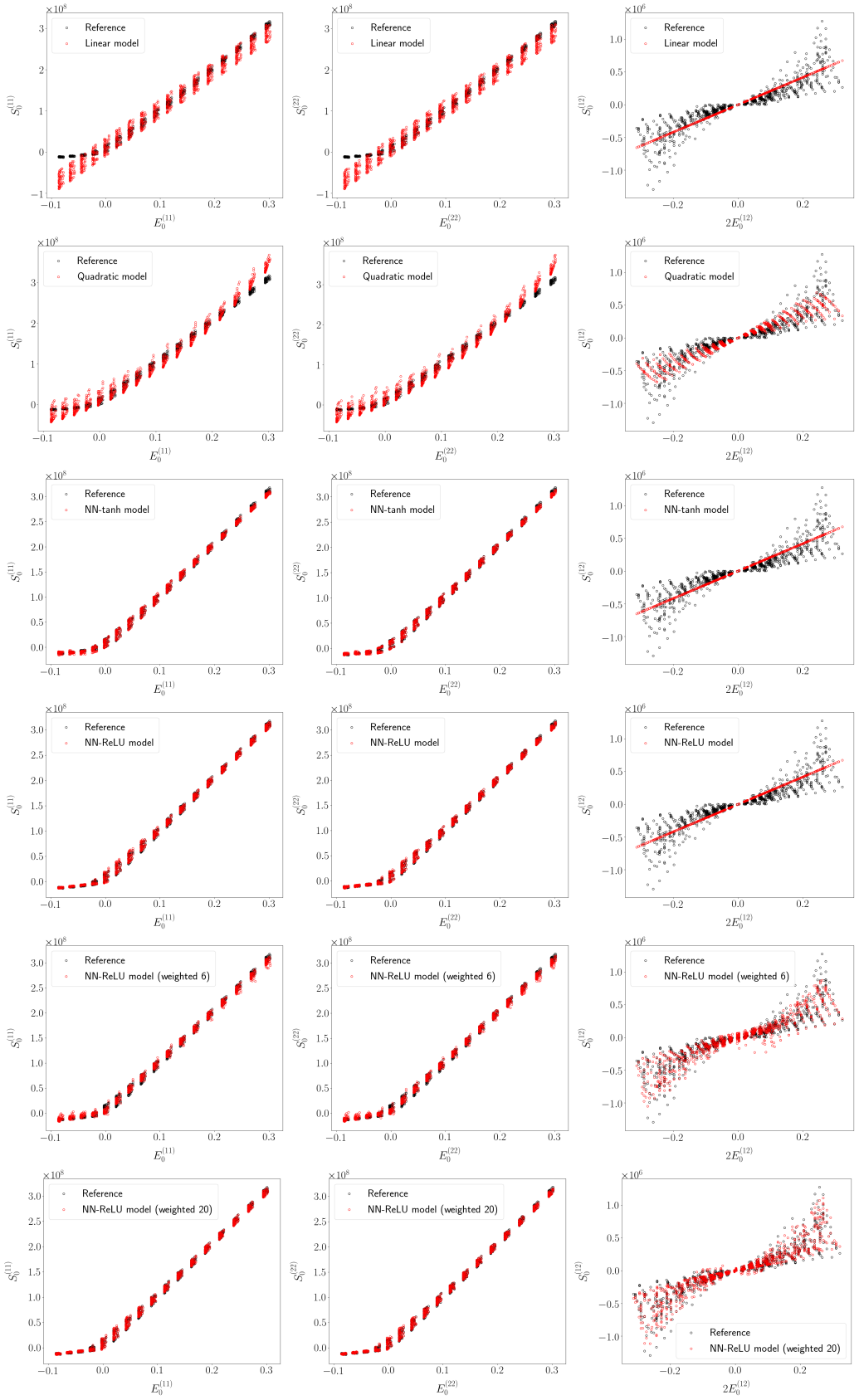

FIGURE 7 Reference and predicted strain-stress pairs for the testing data set.

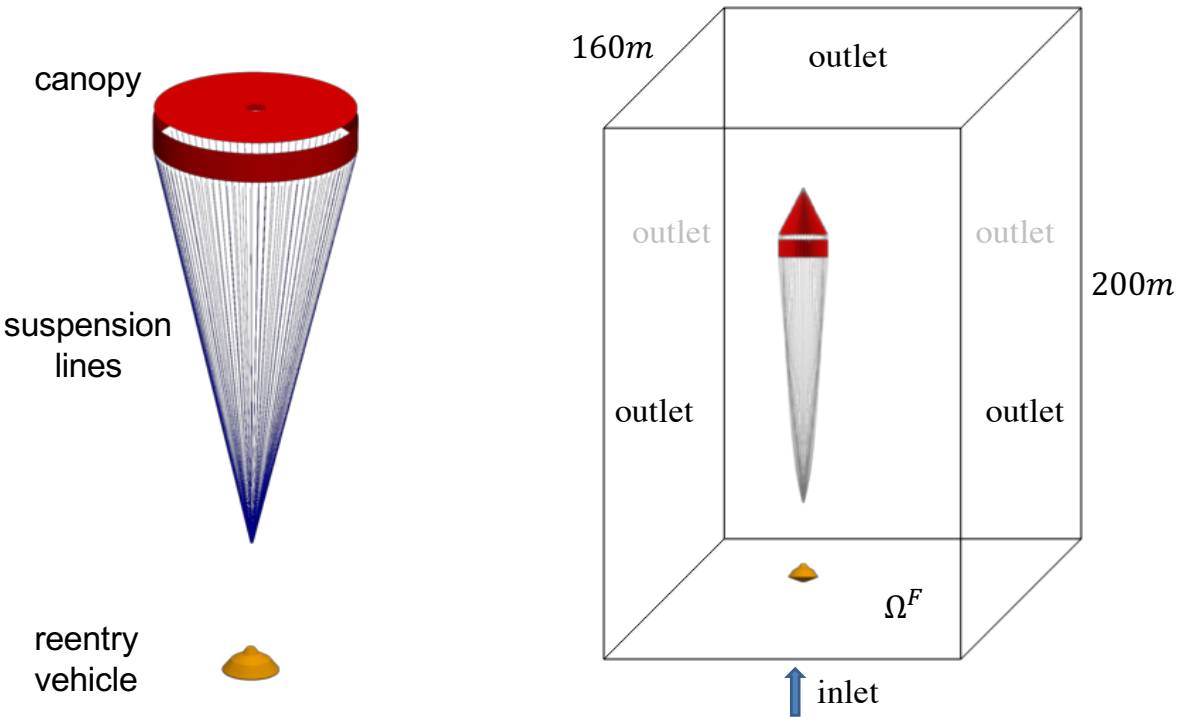

FIGURE 8 Dynamic supersonic parachute inflation problem: system configuration (left); and embedding computational fluid domain as well as embedded initial folded configuration (right).

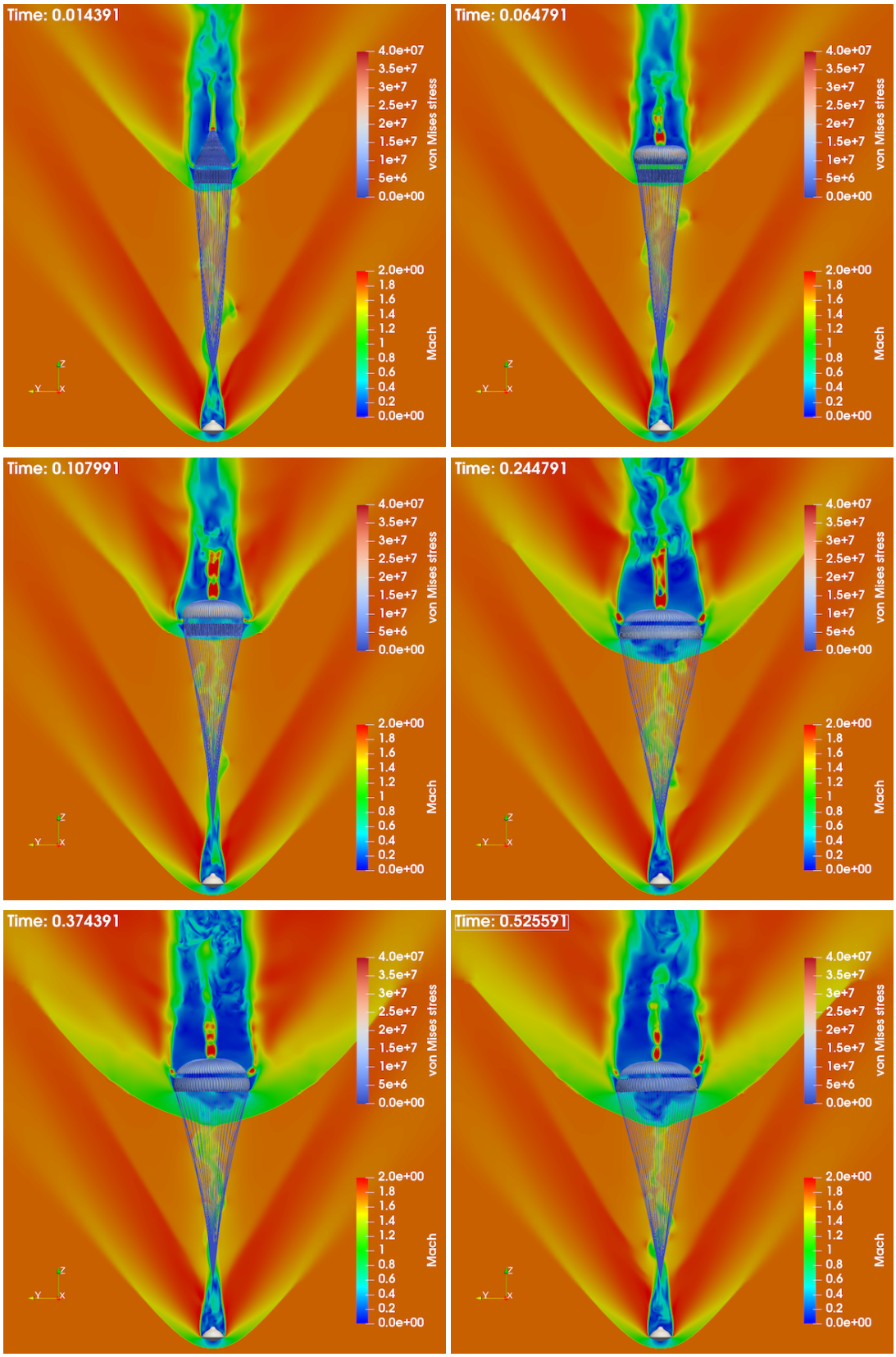

FIGURE 9 Time-evolutions of the deployment of parachute DGB system and the associated flow Mach number field.

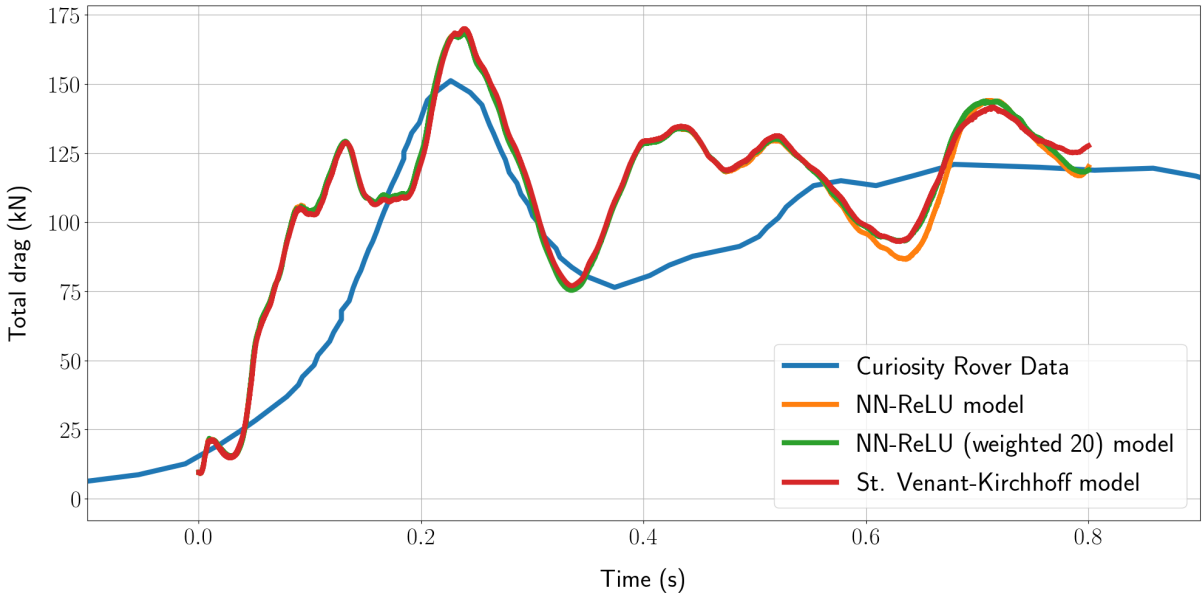

FIGURE 10 Time-histories of the total drag generated during the dynamic, supersonic parachute inflation process: NASA's Curiosity rover data[27] (blue); FSI simulation with the NN-ReLU model-based (orange), NN-ReLU (weighted 20) model-based (green), and St. Venant-Kirchhoff (red) constitutive relations.

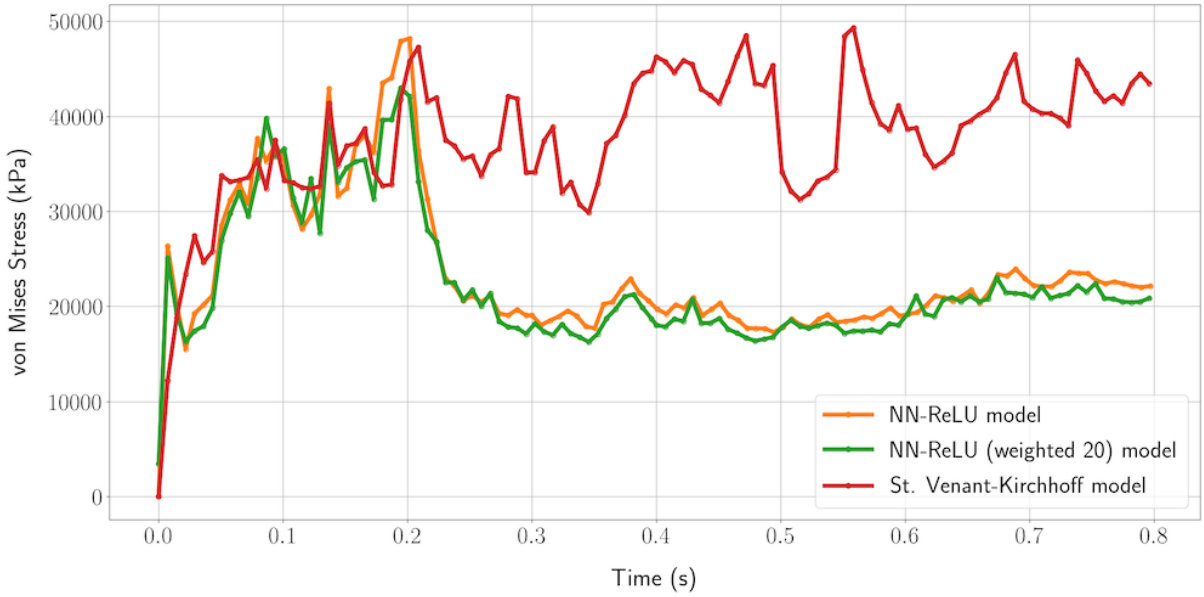

FIGURE 11 Time-histories of the maximum von Mises stresses generated during the dynamic, supersonic parachute inflation process: FSI simulation with the NN-ReLU model-based (orange), NN-ReLU (weighted 20) model-based (green), and St. Venant-Kirchhoff (red) constitutive relations.

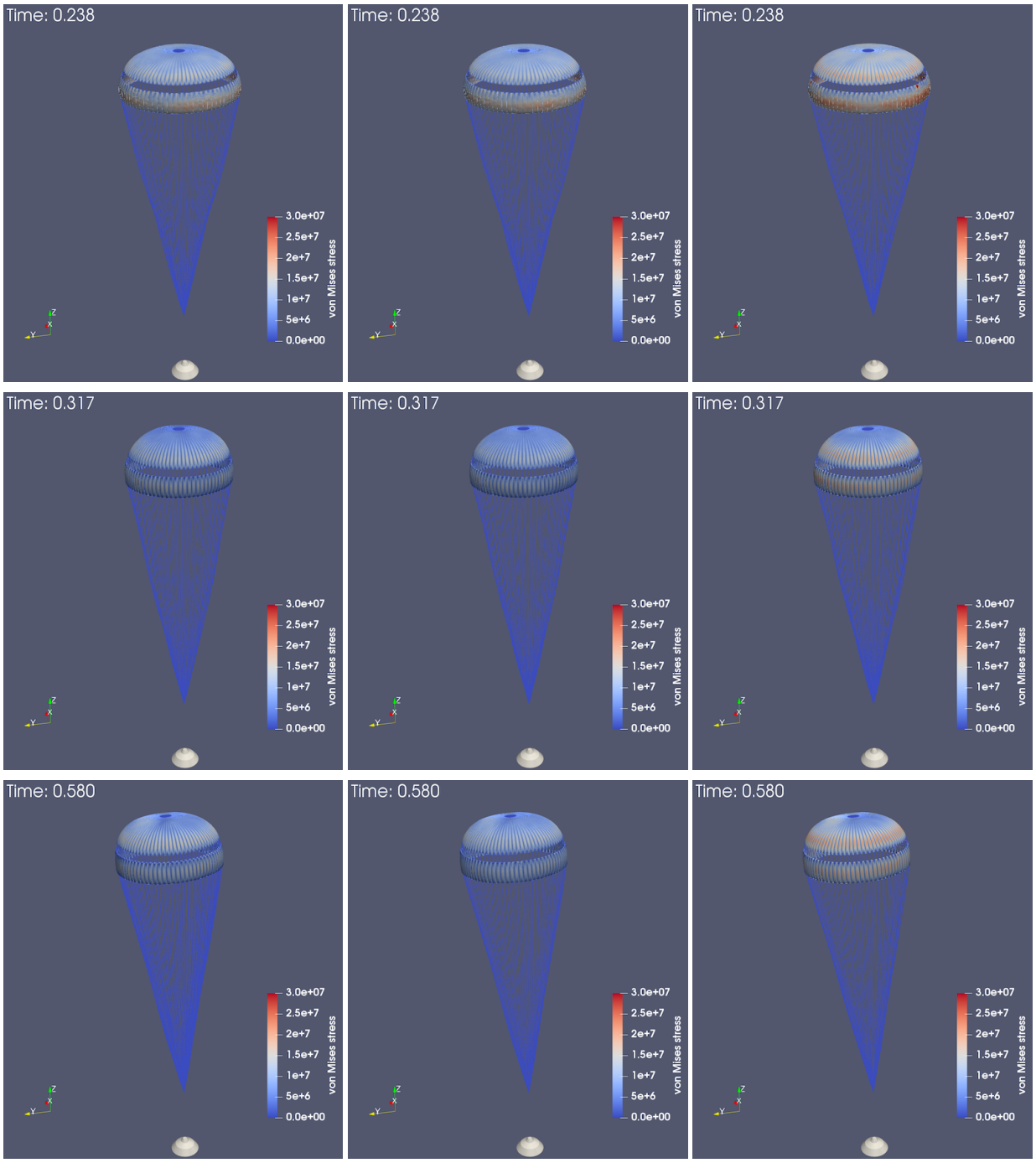

FIGURE 12 Time-evolutions of von Mises stress fields simulated with the NN-ReLU model (left), the NN-ReLU model (weighted 20) (middle), and the St. Venant-Kirchhoff model (right) during the deployment of the parachute DGB system.